

---

Masters Theses

Student Theses and Dissertations

---

Summer 2015

## Freeze-form extrusion fabrication of boron carbide

Aaron Scott Thornton

Follow this and additional works at: [https://scholarsmine.mst.edu/masters\\_theses](https://scholarsmine.mst.edu/masters_theses)

 Part of the [Mechanical Engineering Commons](#)

Department:

---

### Recommended Citation

Thornton, Aaron Scott, "Freeze-form extrusion fabrication of boron carbide" (2015). *Masters Theses*. 7439.

[https://scholarsmine.mst.edu/masters\\_theses/7439](https://scholarsmine.mst.edu/masters_theses/7439)

This thesis is brought to you by Scholars' Mine, a service of the Missouri S&T Library and Learning Resources. This work is protected by U. S. Copyright Law. Unauthorized use including reproduction for redistribution requires the permission of the copyright holder. For more information, please contact [scholarsmine@mst.edu](mailto:scholarsmine@mst.edu).

FREEZE-FORM EXTRUSION FABRICATION OF BORON CARBIDE

by

AARON SCOTT THORNTON

A THESIS

Presented to the Faculty of the Graduate School of the

MISSOURI UNIVERSITY OF SCIENCE AND TECHNOLOGY

In Partial Fulfillment of the Requirements for the Degree

MASTER OF SCIENCE IN MECHANICAL ENGINEERING

2015

Approved by

Ming C. Leu, Advisor

Robert Landers

Gregory Hilmas

©2015

Aaron Scott Thornton

All Rights Reserved

## ABSTRACT

Boron carbide is a safe, alternative to beryllium as a material for aerospace structures since it is also light-weight and exhibits high strength. This paper discusses a study of the Freeze-form Extrusion Fabrication (FEF) process to fabricate parts from boron carbide. Process parameters and hardware were modified to fabricate boron carbide specimens free of printed defects. Four-point bending tests were performed to measure the flexural strength of fabricated specimens. Observations of the presence of voids caused by ice crystals in fabricated parts led to further development and characterization of the boron carbide paste used with the FEF process. Additives were selected and tested to observe their effect on the size of the ice-crystal voids. Scanning electron microscopy was used to observe the voids left from the ice crystals after part sintering. Post-image analysis was performed to measure approximate sizes of ice-crystal voids and these results were summed up in a void size distribution. Glycerol in a concentration of 25 wt% by water increased the flexural strength of test bars from 58.1 MPa to 67.4 MPa and the sintered relative density from 76.2% to 85.0%. The standard deviation of the flexural strength decreased from 23.0 to 14.5 MPa. None of the additives considered reduced the sizes of the ice crystal voids desirably as the highest relative density of the sintered test bars achieved was only 85.0%.

## ACKNOWLEDGMENTS

I give many thanks to my main research advisor Dr. Ming Leu for his guidance and wisdom throughout my graduate studies. I am very grateful for him allowing me to work on the FEF project, as I have learned so much. His generous support was most helpful in obtaining my Master's degree.

I am also deeply indebted to Dr. Landers for all that he taught me about controls and instrumentation. I am grateful for his valuable advice as my co-advisor. I am grateful for him and Dr. Leu helping me to get the GAANN fellowship.

Thank you to Dr. Hilmas for teaching a mechanical engineer so much about ceramics processing. Without his guidance, advice and his laboratory, this work would not have been possible.

A very special thanks goes to Jeremy Watts. He was also invaluable to this work for all of the direct advice and guidance throughout the entire project.

Thank you to Ang Li and Jie Li for all of the background work they performed which provided the valuable foundation which this work continued from. Thank you to Amir Ghazanfari for all of his help throughout this project. Thank you to Maxwell Mulholland for his great help fixing and working on the FEF machine. Thank you to all of my other lab mates which have helped in any way.

Thank you to my wife for her support throughout my time here at school. Her love and support has meant a lot to me. Thank you for being willing to live as a poor graduate student for a while.

## TABLE OF CONTENTS

	Page
ABSTRACT .....	iii
ACKNOWLEDGMENTS .....	iv
LIST OF ILLUSTRATIONS .....	vii
LIST OF TABLES .....	ix
SECTION	
1. INTRODUCTION .....	1
1.1. MOTIVATION .....	1
1.2. RELATED WORK .....	1
1.3. FEF PROCESS OVERVIEW .....	3
2. ADAPTATION OF THE FEF PROCESS FOR BORON CARBIDE .....	4
2.1. CALIBRATION OF PROCESS PARAMETERS .....	4
2.1.1. Estimation of Bead Profile .....	4
2.1.2. Verification of Bead Profile Estimation .....	5
2.1.3. Estimation of Appropriate Raster Spacing .....	11
2.2. TEST BAR FABRICATION .....	15
3. FURTHER DEVELOPMENT OF B <sub>4</sub> C PASTE .....	22
3.1. ADDITIVES .....	22
3.1.1. Selection of Additives .....	22
3.1.2. Development of Test Slurry .....	23
3.2. CONTACT ANGLE .....	24
3.3. FREEZE CASTING OF B <sub>4</sub> C BARS .....	27
3.3.1. Casting Setup and Procedure .....	27
3.3.2. Green and Sintered Densities .....	28
3.3.3. Observation of Ice-crystal Voids .....	30
3.4. RESULTS AND DISCUSSION .....	31
3.4.1. Griffith Criterion .....	31
3.4.2. Ice-crystal Void Size Distribution .....	31
3.4.3. Increasing the Solids Loading .....	48

3.4.4. Comparison of Green and Sintered Relative Densities .....	49
3.5. TEST BARS FABRICATED BY THE FEF PROCESS WITH ADDITIVE .....	52
4. SUMMARY AND CONCLUSION .....	55
5. FUTURE WORK .....	57
APPENDICES	
A. LOW MAGNIFICATION IMAGES (50X ZOOM) OF FREEZE-CAST BARS .....	58
B. SEM IMAGES OF FREEZE-CAST BARS .....	65
C. OTHER ADDITIVES CONSIDERED DURING THE STUDY .....	73
D. RECIPE FOR TEST SLURRY .....	75
BIBLIOGRAPHY .....	78
VITA .....	81

## LIST OF ILLUSTRATIONS

	Page
Figure 1.1 The Triple-extruder Freeze-form Extrusion Fabrication (FEF) Machine Inside the Environmental Chamber .....	3
Figure 2.1 Slab-shaped Bead Cross-Section .....	4
Figure 2.2 Single Rasters Stacked Vertically .....	5
Figure 2.3 Thin-wall Cross-section Frozen too Slowly .....	6
Figure 2.4 Thin-wall Cross-section Frozen at -20o C on an Aluminum Plate .....	7
Figure 2.5 Thin-wall Cross-section Frozen at -20o C, on an Aluminum Plate .....	8
Figure 2.6 Measurements of Thin-wall Cross-sections .....	9
Figure 2.7 Explanation of Inner and Outer Width .....	10
Figure 2.8 Determining the Empty Space Between Beads .....	11
Figure 2.9 Explanation of Offset Rasters.....	13
Figure 2.10 B4C Test Bar Fabricated with the FEF Machine .....	14
Figure 2.11 B4C Test Bar Fabricated with the FEF Machine .....	14
Figure 2.12 Side View of Bar #8 from Table 2.2 .....	19
Figure 2.13 Break Surfaces of Three Bars Printed with Large Diameter Nozzle: .....	20
Figure 3.1 Particle Size Distribution of Boron Carbide Powder .....	23
Figure 3.2 Explanation of Angle $\theta$ .....	25
Figure 3.3 Images used for Contact Angle Measurement.....	26
Figure 3.4 Cross-section View of Mold Setup.....	28
Figure 3.5 50x Zoom Map of Freeze-cast Bar #2 from the 10 wt% by Water Glycerol Group.....	33
Figure 3.6 SEM Image of 10 wt% by Water Glycerol Bar at 350X Zoom .....	34
Figure 3.7 SEM Image of 10 wt% by Water Glycerol Bar at 50X Zoom .....	35
Figure 3.8 Void Size Distribution of 10 wt% by Water Glycerol .....	35
Figure 3.9 Largest Flaw Observed using Optical Microscope in 10 wt% by Water Freeze-cast Bar .....	37
Figure 3.10 50X Zoom Map of Freeze-cast Bar #2 Old from the 20 wt% by Water Glycerol Group .....	38
Figure 3.11 SEM Image of 20 wt% by Water Glycerol Freeze-cast Bar at 60X Zoom ....	39
Figure 3.12 SEM Image of 20 wt% by Water Glycerol Bar at 60X Zoom .....	40



Figure 3.13 Void Size Distribution of 20 wt% by Water Glycerol Freeze-cast Bar .....	40
Figure 3.14 Largest Flaw Observed by Optical Microscope in 20 wt% by Water Freeze-cast Bar .....	42
Figure 3.15 50X Zoom Map of Freeze-cast Bar #3 Old (Table 3.3) from the 25 wt% by Water Glycerol Group .....	42
Figure 3.16 SEM Image of 25 wt% by Water Glycerol Bar at 100X Zoom .....	43
Figure 3.17 SEM Image of 25 wt% by Water Glycerol Bar at 400X Zoom .....	44
Figure 3.18 Void Size Distribution of 25 wt% by Water Glycerol Freeze-cast Bar .....	45
Figure 3.19 Largest Flaw Observed by Optical Microscope in 25 wt% by Water Freeze-cast Bar .....	46
Figure 3.20 Relation Between Solids Loading of Slurry and Relative Sintered Density ..	48
Figure 3.21 Comparison of B4C Freeze-Cast Densities to B4C Iso-pressed Powder Densities.....	49
Figure 3.22 Comparison of B4C Densities with Glycerol Concentration to B4C Iso-pressed Bars .....	51
Figure 3.23 Fracture Surfaces of Flexure Test Bars Printed with 25 wt% by Water Glycerol Concentration .....	53

**LIST OF TABLES**

	Page
Table 2.1 Measured Dimensions vs. Model-predicted Dimensions .....	10
Table 2.2 Flexural Strength and Density of B4C Bars Printed with a Large Nozzle .....	17
Table 2.3 Flexural Strength and Density of B4C Iso-pressed Bars .....	18
Table 3.1 Contact Angles for B4C and Alumina.....	27
Table 3.2 Green Densities of Cast Bars with Various Additives.....	29
Table 3.3 Sintered Densities of Cast Bars with Various Additives .....	30
Table 3.4 Void Size Ranges for Void Size Analysis .....	36
Table 3.5 Comparison of Ice-crystal Voids of Different Glycerol Concentrations .....	47
Table 3.6 Flexural Strength and Densities of FEF Printed Bars with a Glycerol Concentration of 25 wt% by Water .....	52

# 1. INTRODUCTION

## 1.1. MOTIVATION

With a density of  $2.52 \text{ g/cm}^3$  and a potential hot-pressed flexural strength of 480 MPa [1], boron carbide ( $\text{B}_4\text{C}$ ) has a lot of potential use for aerospace structures. Because of its low density it can be used to produce lightweight structures which still exhibit high strength. Currently beryllium is often used in the aerospace industry [2] to manufacture lightweight structures because it is lightweight and exhibits high strength with a density of  $1.844 \text{ g/cm}^3$  and a typical tensile strength of 370 MPa [2]. However, beryllium can be very hazardous to those working with it [3]. Added safety precautions can significantly increase manufacturing costs which are not incurred by other materials. Thus  $\text{B}_4\text{C}$  could be an attractive alternative to beryllium.

## 1.2. RELATED WORK

Recent advances in additive manufacturing have made it possible to fabricate parts from a variety of materials including ceramics. Robocasting typically uses a colloidal gel ink to fabricate parts from a variety of ceramic materials at room temperature [4-5]. 3D printing has been used to fabricate near fully-dense alumina parts with a flexural strength of 320MPa [6], though with 3D printing of ceramics it is very difficult to obtain fully dense parts and post-infiltration is often required to fill in porosity [7]. Selective Laser Sintering (SLS) has been used to fabricate ceramic parts [8], but the SLS process typically produces porous parts causing a decrease in mechanical properties.

This thesis study uses a novel additive manufacturing process called Freeze-form Extrusion Fabrication (FEF) which produces 3-D parts in a layer-by-layer fashion. It extrudes an aqueous-based ceramic-loaded paste from a nozzle onto a substrate in a freezing environment. The freezing of water helps to minimize necessary binder, which makes post processing easier and more environmentally friendly [9-13].

Boron carbide has a relatively high hardness and can only be machined by diamond-coated tooling [1]. Boron carbide is among the hardest materials; the hardness measurements are difficult; the preparation of samples and conditions of measure are uncertain or unknown, therefore values are scattered, and difficult to be compared [1].

This makes subtractive manufacturing an expensive and unattractive method of boron carbide part fabrication. Typical fabrication methods involve hot pressing or pressureless sintering after a green part has been removed from a mold. Hot pressing typically involves temperatures ranging from 2373 – 2473 K and pressures ranging from 30 – 40 MPa for a duration of 15- 40 minutes [1]. Pressureless sintering typically involves powder being packed into a mold in some fashion and then removed from the mold and sintered under an inert gas such as argon or helium. Hot pressing can typically achieve relative densities >99% while pressureless sintering typically can only achieve relative densities of 97% [1]. Hot pressing typically produces flexural strengths of about 480 MPa while pressureless sintering typically achieves flexural strengths of approximately 350 MPa[1].

Li et. al [14] were able to disperse boron carbide powder into water using tetramethylammonium hydroxide (TMAH) as a dispersing agent. They were able to achieve an aqueous slurry with 55 vol% solids loading. However, the paper did not discuss any further processing of the material such as the achieved sintered density or other properties.

Freeze casting is a ceramic mold process which is relevant to the FEF process. Freeze casting does not involve free-form deposition with a nozzle. Instead an aqueous ceramic-loaded slurry is poured into a mold which is then cooled to freezing temperatures. The green part is then removed from the mold and is then freeze-dried to sublime the ice. Next, parts typically go through a binder burnout process and then are sintered. Some researchers have had success with freeze-casting of alumina parts and have used additives such as glycerol to obtain dense parts free of voids leftover from large ice crystals [15].

Prior to this research work had been done to develop a suitable pressureless sintering schedule and development of a paste for  $B_4C$  to be used with the freeze-form extrusion fabrication (FEF) process. This thesis work has added to the previous work by the adaptation of the FEF machine and process to fabricate parts free of printing defects. Additionally, the paste was further developed in an attempt to prevent the formation of ice crystals within parts during fabrication.

### 1.3. FEF PROCESS OVERVIEW

The FEF process uses up to three servo-controlled extruders on a 3-axis gantry to extrude up to three different materials from the same nozzle. Figure 1.1 shows a picture and explanation of the FEF machine. In this research only one material is used: B<sub>4</sub>C paste. The material extruded is an aqueous paste loaded with ceramic powder. It is extruded onto a substrate in a freezing environment to freeze the water in the paste. The part being fabricated becomes rigid once the water freezes. After the part is fully fabricated in a layer-by-layer fashion, it is removed from the cooled environmental chamber and is then freeze-dried. After freeze-drying the part then undergoes binder-burnout, to remove any remaining organic binders, and is then sintered.



Figure 1.1 The Triple-extruder Freeze-form Extrusion Fabrication (FEF) Machine Inside the Environmental Chamber

## 2. ADAPTATION OF THE FEF PROCESS FOR BORON CARBIDE

### 2.1. CALIBRATION OF PROCESS PARAMETERS

**2.1.1. Estimation of Bead Profile.** T. Huang [16] developed a model to relate print parameters with bead cross-section geometry. This model was used to create a consistent bead cross-section with known dimensions. The ideal dimensions can be calculated from Equation (1).

$$V_T = V_E \frac{\pi D_I^2}{4HD_O + \pi H^2} \quad (1)$$

where  $V_T$  (mm/s) is the table velocity,  $V_E$  (mm/s) is the extrudate velocity,  $D_I$  (mm) is the inner diameter of the nozzle,  $D_O$  (mm) is the outer diameter of the nozzle and  $H$  (mm) is the standoff distance or layer height. To use this equation, the user can choose a desired extrudate velocity and a layer height, then from the nozzle geometry, combined with the chosen parameters, the appropriate table velocity can be calculated to achieve a bead cross-section which looks like that of Figure 2.1.

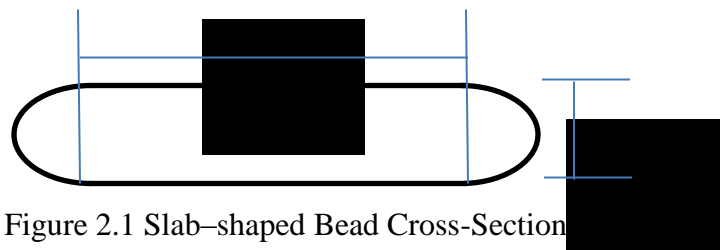
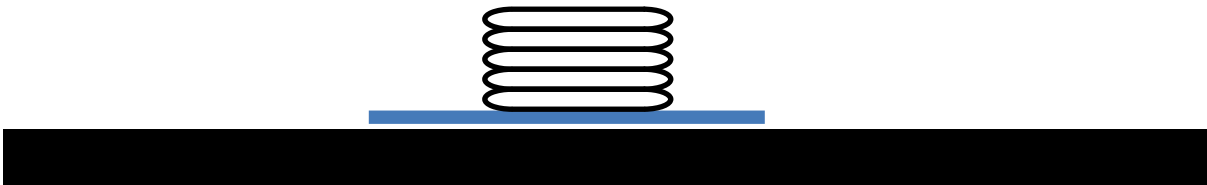


Figure 2.1 Slab-shaped Bead Cross-Section

In Figure 2.1, the slab-shaped bead cross-section is approximated by a rectangle with two half circles on the ends. The height of the rectangle and the diameter of the two

half circles is then  $H$ , the layer height. The width of the rectangle portion can be set as the outer diameter of the nozzle ( $D_o$ ).

**2.1.2. Verification of Bead Profile Estimation.** A few thin-wall parts were printed in order to verify the dimensions of the bead cross-section. These thin walls consist of one single raster printed per layer. Several rasters were stacked on top of each other as shown in Figure 2.2. This thin-wall part was printed five times to account for any variation occurring during the fabrication process. These parts were printed using a nozzle with an inner diameter of 0.580 mm.



After printing, these thin-wall parts were freeze-dried. Next, they were measured using an optical microscope with an attached camera (HiRox HI-SCOPE Advanced KH-3000, Hackensack, NJ). From this analysis it was found that they were frozen too slowly when they were printed at an ambient temperature of  $-15^{\circ}\text{C}$ . This caused the thin-wall parts to melt and deform in such a way that it was impossible to obtain any accurate measurements from the samples. Figure 2.3 shows one such sample.



Figure 2.3 Thin-wall Cross-section Frozen too Slowly

Because the rasters were freezing too slowly and deforming so much it was impossible to detect one raster from another. The thin wall parts were re-printed at a lower temperature of  $-20^{\circ}\text{C}$ . Instead of a plastic sheet, the thin walls were printed directly on top of the aluminum substrate. The lower ambient temperatures forced the thin-wall cross-sections to freeze much faster. Figures 2.4 and 2.5 show cross-sections of thin walls printed under the colder conditions.



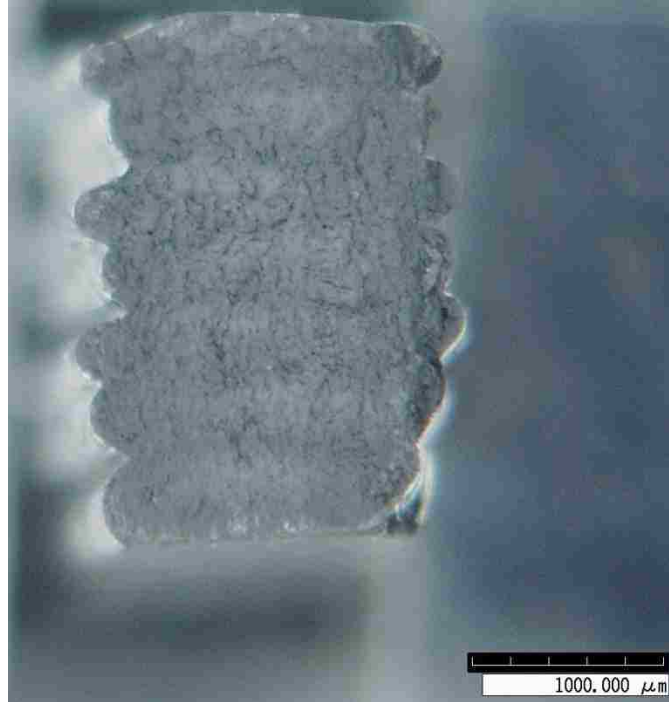


Figure 2.4 Thin-wall Cross-section Frozen at  $-20^{\circ}\text{C}$  on an Aluminum Plate

After analyzing Figure 2.4, it revealed an important flaw in the setup of the 3-axis gantry to which the extrusion system is fastened. As the nozzle extrudes paste, it is not perpendicular to the substrate. Because it is so far from perpendicular (approximately  $2-3^{\circ}$ ) it deforms the bead cross-sections in undesirable ways. One such example is how one layer does not have similar dimensions compared to the next layer above or below. However, all of the odd layers and all of the even layers are similar in geometry to each other.



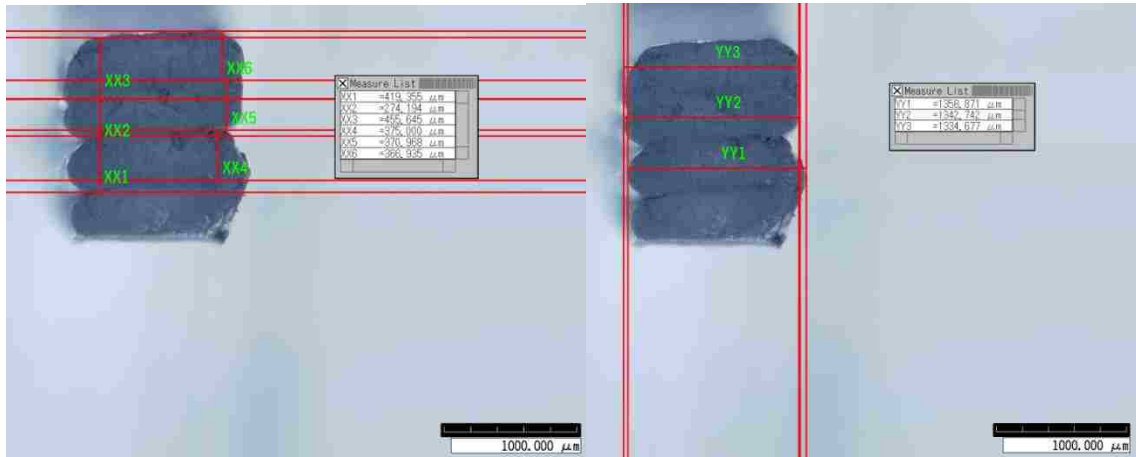
Figure 2.5 Thin-wall Cross-section Frozen at  $-20^{\circ}\text{C}$ , on an Aluminum Plate

The ideal bead profile as shown in Figure 2.1 is a slab with a flat top. The top layer in Figure 2.5 is not flat. This is also due to the extrusion nozzle not being perpendicular to the substrate. The model as shown in Equation (1) requires the extrusion nozzle to deform the paste as it is extruded. Ideally the outer edges of the end of the nozzle actually push the paste flat. In the case of Figure 2.5, the nozzle is digging into the paste causing repeated valleys and hills instead of a flat surface.

In order to address this issue, the nozzle was made perpendicular to the substrate. New hardware was constructed and the 3-axis gantry was re-aligned to the substrate to ensure that the nozzle truly was perpendicular to it.

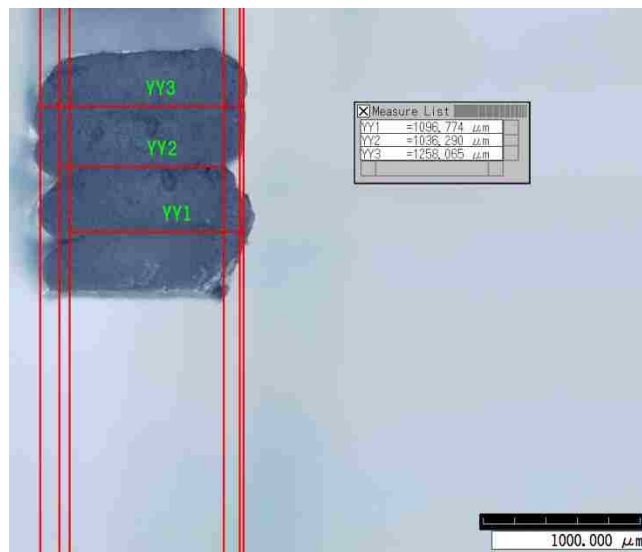
After aligning the gantry system so that the extrusion nozzle was perpendicular ( $< 0.001$  in/in) the thin walls were re-printed. It can be seen in Figure 2.6 that the re-printed thin walls did not suffer from the obvious problems caused by a non-perpendicular extrusion nozzle. Measurements of individual bead cross-sections were taken: height,

outer width and inner width. Figure 2.7 shows the difference between the outer and inner width of the beads.



a)

b)



c)

Figure 2.6: Measurements of Thin-wall Cross-sections  
 a) Measurements of Height  
 b) Measurement of Outer Width  
 c) Measurement of Inner Width

The measurements shown in Figure 2.6 were taken on the HiRox optical microscope. The software on the microscope allows for lines to be drawn on top of the specimen being viewed. These lines can be used to determine distances. The red lines in Figure 2.6 are such lines. The software on the microscope was used to draw these lines and measure the dimensions of the bars. The measurements of the bars are summed up in Table 2.1.

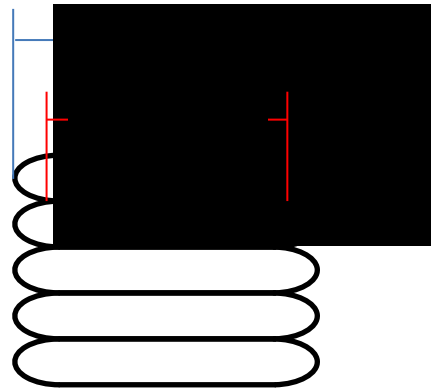


Figure 2.7 Explanation of Inner and Outer Width

Table 2.1 Measured Dimensions vs. Model-predicted Dimensions

Prediction of Raster Spacing From Measurements		Prediction of Raster Spacing From Model	
Desired Raster Spacing (in)	0.0573	Raster Spacing (in)	0.0466
Desired Raster Spacing (mm)	1.4565	Raster Space (mm)	1.1842
L (mm)	0.3142	L (mm)	0.3142
H (mm)	0.4000	H (mm)	0.4000
Average Inner Widths (mm)	1.1423	$D_o$ (mm)	0.8700
Average Outer Widths (mm)	1.3634	Calculated Outer Width (mm)	1.2700
$D_i$ (mm)	0.5800	$D_i$ (mm)	0.5800

Figure 2.6 is just one example of the four individual thin walls that were used to obtain the data in Table 2.1. The outer width, inner width and height of each bead cross-section, except the very bottom, within each bar were measured. In total 23 individual bead cross-sections were measured.

The average outer width of all the bead cross-sections printed was  $1.3643 \pm 0.013$  mm. The average inner width was  $1.1423 \pm 0.0977$  mm. The average height of the bars was  $0.397 \pm 0.0347$  mm.

**2.1.3. Estimation of Appropriate Raster Spacing.** When two beads are placed side-by-side the area between them can be calculated with some simple geometry. This can be done by drawing an imaginary box around the space between the beads as shown in Figure 2.8. The red-dashed box is the imaginary box. The area of this box is the standoff distance  $H$ , multiplied by an arbitrary distance denoted as  $L$  but is fixed where the rectangle and the circle of the bead cross section meet tangentially. The area not filled in by paste is  $A_L$ . Since it is desired that this area is to be filled,  $A_L$  is set to zero and the equation is solved in terms of  $L$  using Equation (2).

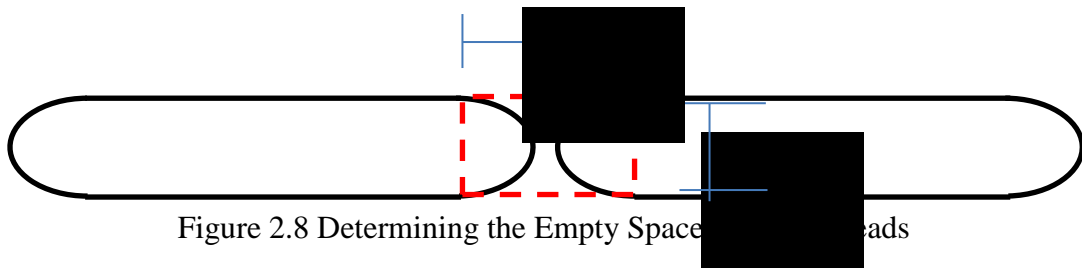


Figure 2.8 Determining the Empty Space between beads

$$A_L = LH - \frac{\pi}{4} H^2 \quad (2)$$

$$L = \frac{\pi}{4} H \quad (3)$$

The appropriate raster spacing is then calculated by adding  $L$ , from Equation (3), and the width of the rectangular section. Equation (1) suggests that the width of the rectangular portion should be  $D_o$ . However as shown in Table 2.1 it is not as can be seen by the data from the measurements.

The data gathered from measuring the thin-wall cross-sections, as shown in Figure 2.6 and Table 2.1, shows that the beads were wider than the model predicted. As shown in Table 2.1, the average inner width of the bead cross sections was 1.1423 mm while the model predicted this was to be 0.8700 mm (the measured outer diameter of the nozzle or  $D_o$ ). Since the inner width and  $D_o$  were used to calculate the desired raster spacing both methods predict rather different spacings. The measurements suggest that the appropriate raster spacing should be 1.4565 mm. The model predicts an appropriate raster spacing of 1.1842 mm.

The most likely reason the width of the rectangular section in actual printing is wider than what the model predicted, in Table 2.1, is due to machine error. On the FEF machine, the paste velocity is controlled by setting a reference velocity for the ram. The model assumes a truly constant paste extrusion rate exactly at the reference rate. In reality the extrusion controller may cause error in the extrusion velocity (deviation from the reference velocity) and non-constant extrusion rates due to paste extrusion dynamics. A change in the extrusion rate would change the dimensions of the extrudate cross-section.

Five test bars were made according to the raster spacing suggested by the prediction made by the measurements from Table 2.1. They were printed with a nozzle with an inner diameter of 0.58 mm. The layers were offset from each other by one-half of a raster width. For example, layer 1 was 9 rasters wide while layer 2 was only 8 rasters wide. The rasters laid down in layer 2 were not laid directly on top of layer 1, but shifted over by one-half of a raster width so that they would lie on top of but in between the two rasters below in layer 1. This was done in the same fashion that a brick mason typically lays down bricks. Figure 2.9 helps further explain how this was done.

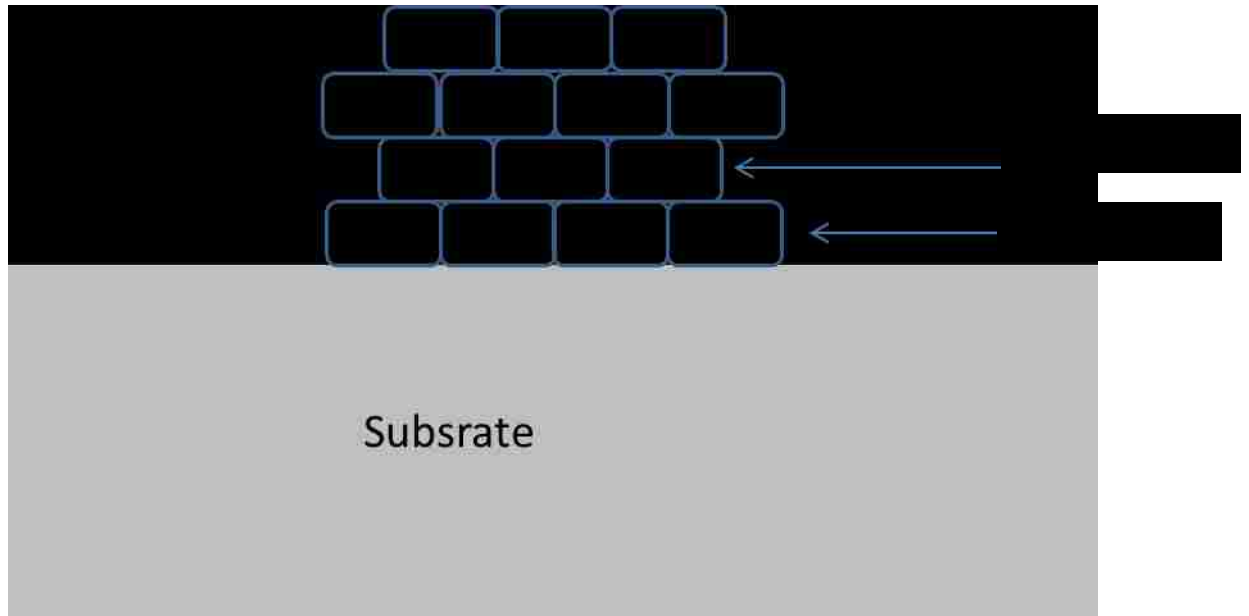


Figure 2.9 Explanation of Offset Rasters

Initially these test bars were fabricated according to the raster spacing suggested by the predictions made by the measurements from Table 2.1. This spacing produced bars with desirable cross sections; viewing the cross sections with the naked eye revealed no visible pores between beads suggesting that the beads were packed together tightly, filling any possible voids between them. Because of these good results several bars were printed with the intention of flexure-testing them. After these bars were printed, a few of them were broken by hand in the green state and their cross sections were examined under the HiRox optical microscope. Figures 2.10-2.11 show two of these cross-sections.



Figure 2.10 B<sub>4</sub>C Test Bar Fabricated with the FEF Machine

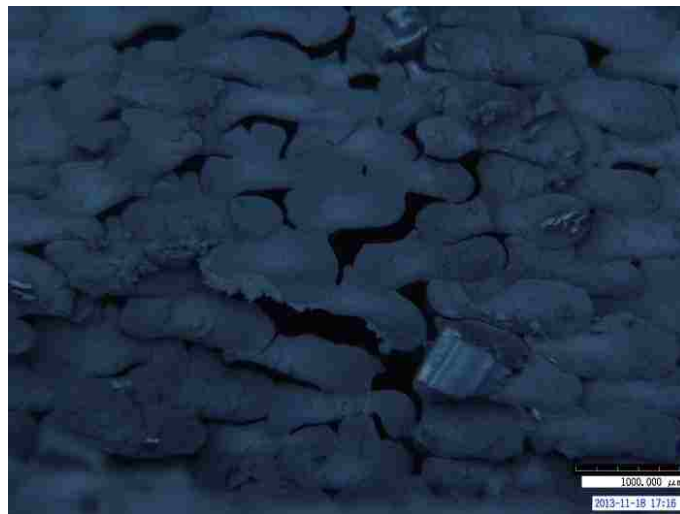


Figure 2.11 B<sub>4</sub>C Test Bar Fabricated with the FEF Machine

Figure 2.10 shows the cross-section of a bar that is free of inter-bead voids. However, there are ice-crystal voids throughout the cross-section which can be just as detrimental to the density and strength of the bar as the inter-bead voids. Figure 2.11 shows another bar printed with the same print parameters as that of Figure 2.10.



However, it shows rather different results. There are many voids between the beads. Up until this point it was unknown what would cause this to occur. The temperature of the substrate which the parts were built upon had not been measured up to this point.

After monitoring the temperature of the substrate with an attached thermocouple it was found why the difference occurs. The bar in Figure 2.10 was built when the air temperature reached  $-23^{\circ}\text{C}$ , but the substrate was above this temperature. The bar in Figure 2.11 was built at a later time which allowed the substrate to reach a steady-state temperature. A substrate which is too warm ( $> -17^{\circ}\text{C}$ ) results in a nice uniform cross-section but with large ice crystals. A substrate temperature that is too cold ( $< -21^{\circ}\text{C}$ ) results in inter-bead voids, but ice crystals do not appear to be forming.

## 2.2. TEST BAR FABRICATION

It was decided to use a nozzle with a much larger diameter (3mm inner diameter) to print test bars. A large nozzle extruding beads of much larger dimensions than the smaller nozzle (0.58 mm inner diameter) would require fewer beads to fill the same volume to fabricate a bar. If fewer beads are required then there would be fewer interfaces between beads which would reduce the chances for voids to occur between beads.

In order to print bars with good mechanical properties it was desired to avoid the formation of large ice crystals. Figure 2.10 shows a bar printed under conditions which apparently reduced the size of ice crystals. It was thought that if the bars were printed with the big nozzle under the same conditions, then the formation of large ice crystals could be avoided. Thus, the bars were printed with a large nozzle at an environment temperature of  $-23^{\circ}\text{C}$  and a substrate temperature of  $-19^{\circ}\text{C}$ . These conditions closely mimic the environmental conditions under which the bar from Figure 2.10 was printed.

The raster spacing was set to 3.4493 mm (0.1358 inches). The extrusion rate was not directly measured but the reference speed of the ram was set to 0.02 mm/s. The table speed was calculated from Equation (1), which resulted 7.44 mm/s (17.58 ipm). The toolpath followed a simple rectangle which was only two rasters wide per layer. After the rectangle was printed the nozzle would raise one layer height (400  $\mu\text{m}$ ) and print a new rectangle. The bars were printed to 30 layers in height (12 mm).

The bars printed with the large nozzle (3mm inner diameter) were post-processed like all the other boron carbide specimens fabricated with the FEF process. They were freeze-dried at  $-20^{\circ}\text{C}$  for 72 hours. Then, they were pressurelessly sintered in helium gas. First, the initial ramp was from room temperature to  $1350^{\circ}\text{C}$  at a rate of  $30^{\circ}\text{C}/\text{min}$  and held until the vacuum returned to 200 mTorr. Next, the temperature was increased to  $1650^{\circ}\text{C}$  also at a rate of  $30^{\circ}\text{C}/\text{min}$  and held until the vacuum pressure returned to 200 mTorr. These two holds were done to remove any  $\text{B}_2\text{O}_3$  which may have been on the surface of the powder. While the borate would off-gas, the vacuum pressure would increase a bit. Rather than trying to measure how long these holds should have been performed, the sintering program was held manually until vacuum pressure returned. After these holds the temperature was increased also at a rate of  $30^{\circ}\text{C}/\text{min}$  until  $2230^{\circ}\text{C}$  was reached and then was held for 30 minutes [17].

For flexural testing, the bars were cut and ground to ASTM C1161-02b standards on a four-point bending fixture on a mechanical load frame (Instron, 5881, Norwood, MA). Table 2.2 shows the results of the flexure testing. Table 2.3 shows the results of the flexure testing of iso-pressed powder bars fabricated and tested prior to this work [17].

Table 2.2 Flexural Strength and Density of B<sub>4</sub>C Bars Printed with a Large Nozzle  
(3mm inner diameter)

Specimen	Flexural Strength (MPa)	Maximum Flexure Load (N)	Relative Density
1	105.4	140.3	0.764
2	69.9	91.4	0.781
3*	N/A	N/A	0.740
4*	N/A	N/A	0.770
5	33.1	44.2	0.794
6	51.0	67.4	0.745
7	87.3	112.5	0.752
8	52.8	68.7	0.738
9	73.4	97.4	0.760
10	28.4	33.1	0.754
11	55.8	75.5	0.749
12	31.6	41.9	0.773
13	50.9	64.4	0.772
Average	58.1	76.1	0.762
Standard Deviation	23.0	30.8	0.016

\* These specimens broke during loading into the testing machine and their flexural strength was not measured

As shown in Table 2.2, the average flexural strength of the test bars was 58.1 MPa with an average sintered relative density of 76.2%. The standard deviation of the flexural strength was 23.0 MPa.

Table 2.3 Flexural Strength and Density of B4C Iso-pressed Bars [17]

No.	Flexure stress at Maximum Flexure load (MPa)	Young's Modulus (GPa)	Relative Density After Sintering
1	241.5	296.9	0.874
2	264.3	304.4	0.885
3	283.8	305.2	0.880
4	232.3	306.1	0.884
5	227.9	291.4	0.879
6	273.9	299.8	0.889
7	255.6	284.8	0.884
8	266.6	294.7	0.882
9	257.4	299.3	0.889
10	277.2	332.3	0.888
11	221.2	341.2	0.881
12	246.6	330.3	0.887
13	254.9	326.8	0.878
14	269.3	317.1	0.890
Mean	255.2	309.3	0.884
STD	18.4	16.7	0.005

The average flexural strength of the iso-pressed powder bars was 255.2 MPa with an average sintered relative density of 88.4%. The standard deviation of the flexural strength was 18.4 MPa.

The resulting flexural strength of the FEF bars is rather low when compared to the iso-pressed bars prepared prior to this work [17]. This low strength can be attributed to two reasons. First, there were still voids left from ice crystals in the bars. Figure 2.12 is a picture of bar number 8 from Table 2.2 which shows these voids.

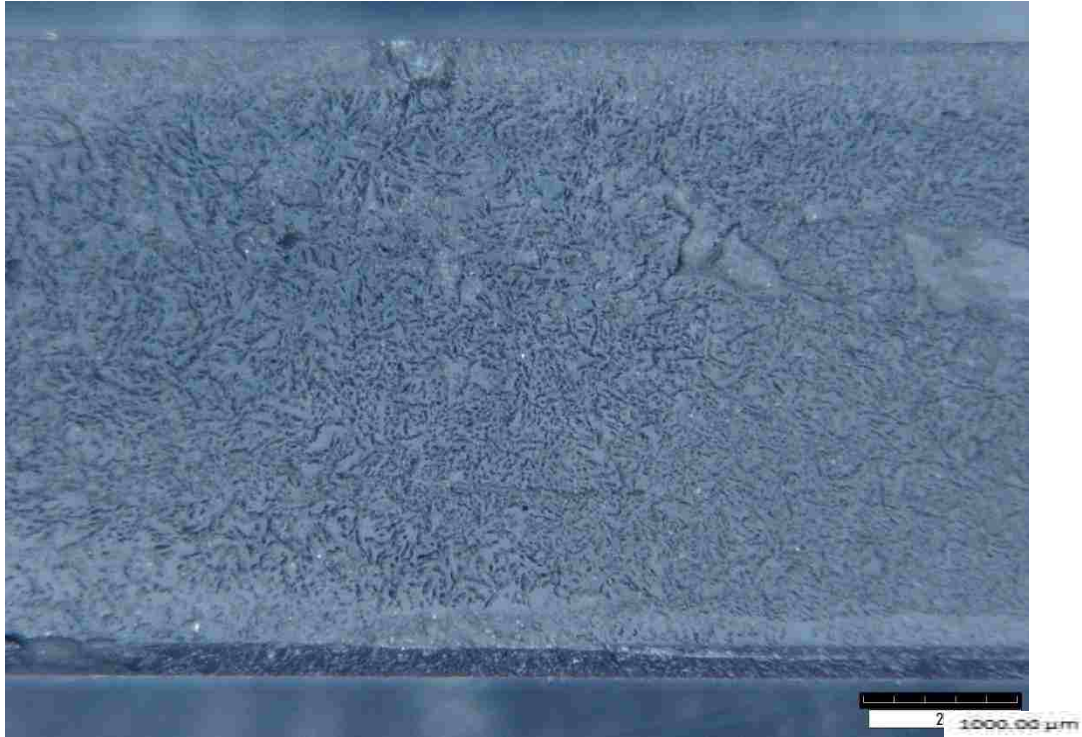
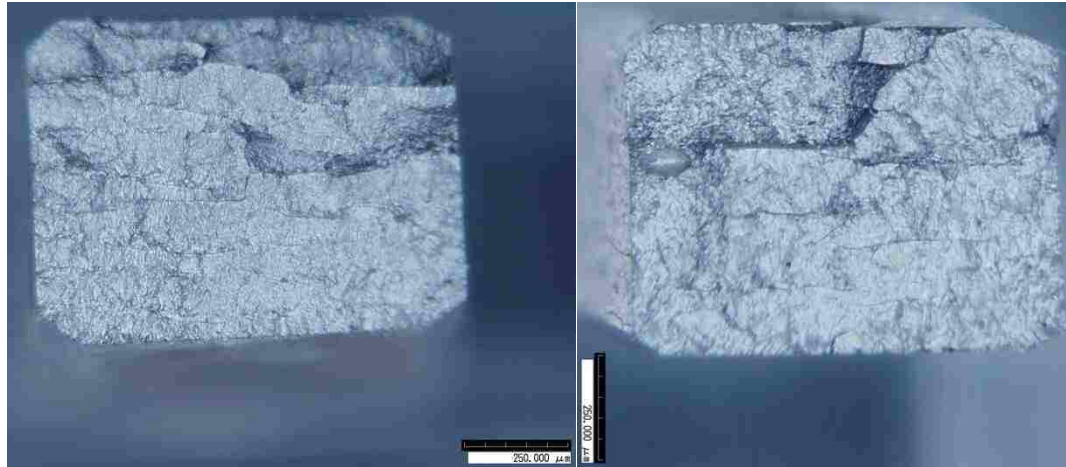


Figure 2.12 Side View of Bar #8 from Table 2.2

Figure 2.12 was taken on the HiRox optical microscope. It shows lots of large pores caused by the formation of large ice crystals. These voids create many crack initiators and decrease the relative density of the bar.

The second reason the bars exhibit such low flexural strength is due to poor inter-layer bonding. During the grinding process entire layers would de-laminate from each other. When the bars were broken they would not form a clean break surface like a properly dense and properly strong bar should. Rather, they fractured along the seam between layers causing many splinters much like a piece of wood. Pictures of the break surfaces were taken to observe any possible voids between layers or beads. Figure 2.13 shows pictures of three of the bars.



(a)

(b)



(c)

Figure 2.13 Break Surfaces of Three Bars Printed with Large Diameter Nozzle:  
a) Bar #3; b) Bar #8; c) Bar #11 (from Table 2.2)

Figure 2.13 shows three bars from the group of broken bars from Table 2.2. They all show desirable cross-sections because there are no voids between beads or between layers caused by the printing process. This suggests that the extrusion rate, table speed, and raster spacing are appropriate. Picture C from Figure 2.13 shows what look like might be voids. These are not voids but are caused by pull-out when the bar was broken.

Since there were no inter-bead voids observed in the large nozzle bars the printing parameters were appropriate. Therefore, the most important concern with these bars was the presence of the ice-crystal voids. If the size of the ice crystals could be significantly reduced then the density would increase significantly.

### 3. FURTHER DEVELOPMENT OF B<sub>4</sub>C PASTE

#### 3.1. ADDITIVES

Since large pores due to ice-crystal formation could not be avoided during the printing process, it was desired to try to eliminate these ice crystals causing the large voids. Various additives were researched to determine if they would be suitable for addition to the paste. The following were selected as additives; alumina (Almatis A16SG), aquazol (Aquazol 5, Polymer Chemistry Innovations, Inc., Tucson, AZ), glycerol (ACROS product #15892-0025), BYK 348 and BYK 349 (BYK Additives and Instruments, Germany). Recipes including the concentrations of each of these additives are in Appendix D.

**3.1.1. Selection of Additives.** Aquazol was previously used as a thickening agent in paste with the FEF process before the introduction of methylcellulose [10]. It was desired to test the slurry with aquazol as an additive to determine if the difference between it and methylcellulose has an effect on ice-crystal nucleation.

Since the alumina paste does not show signs of large ice-crystal formation, it was decided to select alumina as an additive to be tested. It was thought that since alumina apparently nucleates ice more efficiently than boron carbide, adding some alumina powder to the boron carbide paste might help increase the ice nucleation efficiency. Glycerol was selected because of its success with another research group trying to eliminate ice crystals in an alumina slurry with the freeze casting process [15]. Thus it was decided to try glycerol in various amounts (10, 15, 20, 25 wt% by water) to try and reduce the ice-crystal sizes. Weight% by water means that a portion of the water is replaced by glycerol. For example, if the total weight of the fluid is 100g, then 25g of glycerol and 75g of water would be a glycerol concentration of 25 wt% by water. BYK 348 and BYK 349 are both surfactants produced by BYK and were suggested as additives by their chemists. Ideally these surfactants would form micelles within the paste which would prevent the formation of large ice crystals. These two surfactants were used as additives in the slurry.



**3.1.2. Development of Test Slurry.** The powder used in this study is grade HD 20 from H.C. Starck. A particle size analysis was performed on the powder to determine the particle size distribution. The particle size and size distribution analysis were performed using the Microtrac Particle Size Analyzer (S3500, Microtrac, Montgomeryville, PA). The user inserts the powder in question into the machine and specifies what the powder is. After a specific size range desired to be tested is specified to the machine it gives the results of the test. The average particle size was  $0.37\ \mu\text{m}$ . Figure 3.1 shows the results of the particle size analysis and the particle size distribution. The y-axis shows %Chan which means the percentage of particles at that size. For example, approximately 5% of the particles examined are  $0.5\ \mu\text{m}$  in size.

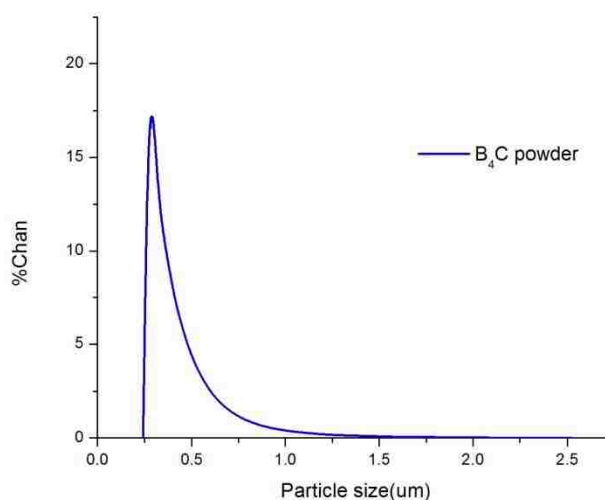


Figure 3.1 Particle Size Distribution of Boron Carbide Powder

The slurry consists of de-ionized water, washed powder, TMAH (tetramethylammonium hydroxide) as a dispersant, and one of the additives. The B<sub>4</sub>C powder was washed in methanol before being used to make paste. This was done to

remove any borate which may have been on the surface of the powder. The first step in making the slurry is to add the dispersant, TMAH, to the water while being stirred by a mixer. Once the TMAH dissolves into the water the powder can be added slowly. After the powder is added then the additive can be added. The slurry was typically left to mix for approximately fifteen minutes once all components had been added. After this mixing was done the slurry was moved to a whip-mix container where it was whip-mixed for 5, then 3, then 2 minutes taking 2 minute breaks in between. The slurry was whip-mixed to remove any air which may have been dissolved into the slurry. This helps eliminate the presence of air bubbles in finished parts. The control slurry was made in the same manner except that no additive was mixed in. The solids loadings of all slurries were 50 vol%  $\pm$  1%.

Typically when a paste is made for printing with the FEF process it is thickened with methylcellulose. For the purposes of the casting performed in this study no methylcellulose was added to any slurry. Different additives affected the viscosity of the slurry in different ways. This would have required a different amount of methylcellulose for each additive in its slurry. The methylcellulose was not added in order to keep each batch of slurry consistent with the rest, and to avoid time-consuming calibration of an appropriate amount of methylcellulose for each additive.

### 3.2. CONTACT ANGLE

In research performed by Fletcher [16] it was shown that the contact angle between water and small particles immersed in that water can affect the way the water nucleates onto those particles in the form of ice. Fletcher proposed a theory that relates the surface energy between the liquid water, ice, and the particle to the contact angle via Equation (4)

$$m = \cos\theta = \frac{(\sigma_{pw} - \sigma_{pi})}{\sigma_{iw}} \quad (4)$$

where  $\theta$  is the contact angle,  $\sigma_{pw}$  is the relative surface energy between the particle and water,  $\sigma_{pi}$  is the relative surface energy between the particle and ice, and  $\sigma_{iw}$  is the

relative surface energy between ice and water. The parameter  $m$  can then be related to a theoretical threshold temperature for ice nucleation with varying sizes of particle nuclei. Figure 3.2 shows how  $\theta$  is defined.

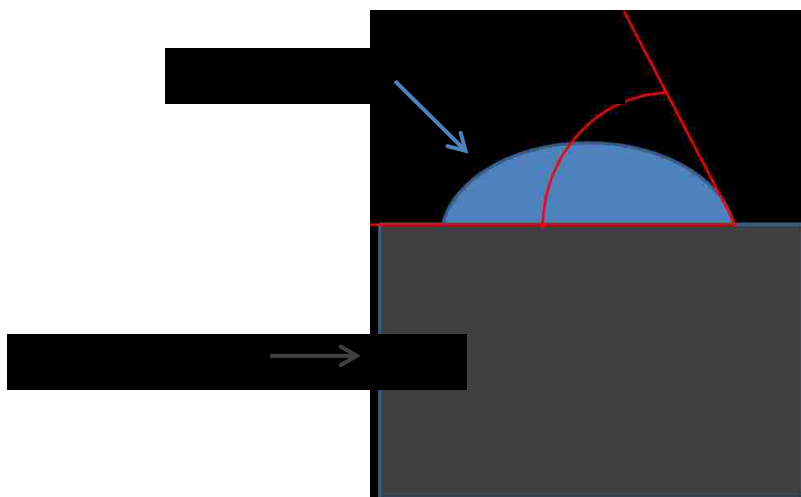


Figure 3.2 Explanation of Angle  $\theta$

Materials with relatively high surface energy have a relatively low contact angle and should nucleate ice efficiently. Materials with a relatively low surface energy typically have a relatively high contact angle and nucleate ice inefficiently. It was thought that the  $B_4C$  powder being used most likely had a high contact angle. This high contact angle would reduce the wetting of the water on to the particles and therefore reduce the ice-nucleation efficiency. Thus, it was desired to observe the contact angle between water and  $B_4C$ .

Parts fabricated with the FEF process from alumina paste do not exhibit signs of ice-crystal voids. It was desired to compare the contact angle of the alumina powder to that of the  $B_4C$ . Both material types were prepared by isostatically pressing a cylindrical pellet at approximately 30,000 psi and then sintering them. The  $B_4C$  pellet was sintered following the sintering schedule described in section 2.2. The alumina pellet was sintered

in air with a ramp of  $10^{\circ}\text{C}/\text{min}$  up to  $1550^{\circ}\text{C}$ , and held for one hour. After sintering, the top surface of both specimens was polished to  $0.25\ \mu\text{m}$  surface finish.

Typically contact angle measurements are done with commercially available machines. These machines can account for the hysteresis of the measurement and can calculate an equilibrium contact angle. Since no such machine was available, this experiment was performed with a pipette and a camera. Figure 3.3 shows a sample picture of a specimen with a drop of water on it. Multiple measurements were taken and averaged in order to account for the hysteresis and experiment variation. The pictures were then imported into Image J (<http://imagej.nih.gov/ij/index.html>) where the approximate contact angle was measured. The results of this test are shown in table 3.1.

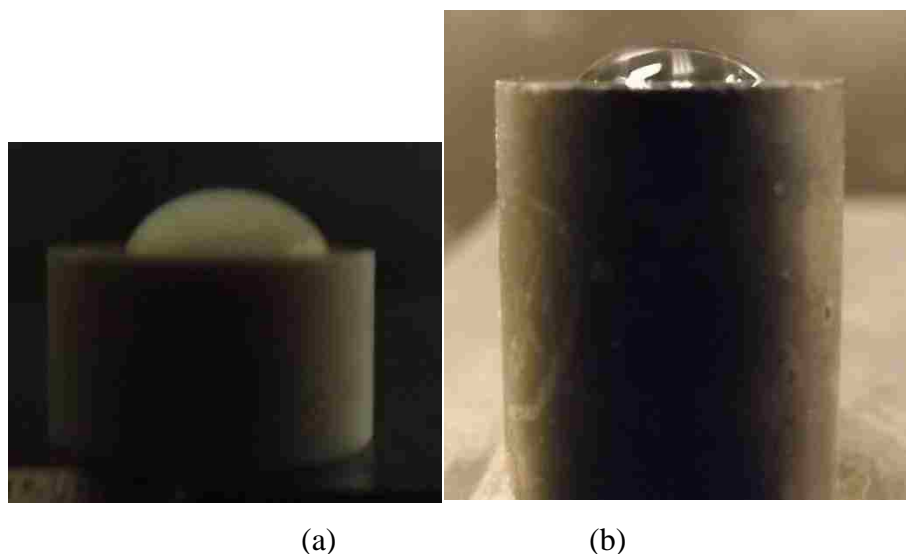


Figure 3.3 Images used for Contact Angle Measurement of; (a) Alumina Sample; (b)  $\text{B}_4\text{C}$  Sample

Table 3.1 Contact Angles for B<sub>4</sub>C and Alumina

Test #	Material Angle (Degrees)	
	B <sub>4</sub> C	Alumina
1	40	49
2	41	49
3	38	53
4	41	55
5	41	54
Average	40	52

The resulting contact angles as shown from Table 3.1 are not what were expected. It was thought that the contact angle of the alumina sample would be smaller than that of the B<sub>4</sub>C since alumina appears to be more efficient at nucleating ice crystals. However, as observed in Table 3.1 the B<sub>4</sub>C sample actually has a smaller angle than the alumina sample. A low contact angle suggests good wetting and high surface energies, which is desirable for ice nucleation according to Fletcher [18]. These results suggest that poor ice-crystal nucleation with the B<sub>4</sub>C powder is not caused by surface energy. Instead, poor ice-crystal nucleation is most likely caused by the surface chemistry.

### 3.3. FREEZE CASTING OF B<sub>4</sub>C BARS

**3.3.1. Casting Setup and Procedure.** After a batch of slurry was made it was taken to the FEF machine and cast inside the FEF environmental chamber under the same freezing conditions used for printing typical B<sub>4</sub>C paste with an environmental temperature of -20°C. A mold made of Teflon was used to cast bars of the various B<sub>4</sub>C slurries. This mold was left in the freezing conditions until it reached -19°C, which was the same temperature as the substrate they were cast on. Figure 3.4 is a cross-section view which helps explain the mold setup.



Figure 3.4 Cross-section View of Mold Setup

The mold was made of Teflon. It was laid upon the top of the aluminum substrate which parts are typically fabricated upon. Above the mold and the cast slurry was the air inside the environmental chamber.

The slurry was left in the mold to freeze until it was solid to the touch. Once solid it was removed from the FEF environmental chamber, while still in the mold, and placed into the freezer in the lab where it was kept at  $-20^{\circ}\text{C}$ . It was kept in this freezer for at least 6 hours to ensure the bar was completely frozen but no more than 24 hours.

**3.3.2. Green and Sintered Densities.** The green specimens went through a binder burnout run in a furnace. This binder burnout was done by ramping up the oven from room temperature to  $1350^{\circ}\text{C}$  at a rate of  $30^{\circ}\text{C}/\text{min}$  and held until vacuum was achieved. Once the binder burnout was finished their density was measured via Archimedes' method using acetone as a medium instead of purified water. Acetone was used in an attempt to minimize degradation of the green samples since it was anticipated that the parts would be damaged and degraded once submerged in water. The green density results are shown in Table 3.2. Three specimens were measured in each additive group. In Tables 3.2 and 3.3 the specimens noted as "old" refer to a tub of paste which was a few days older (6-7) than the specimens marked as "new". Within these Tables 3.2 and 3.3 the term % glycerol refers to wt% by water.

When the green parts were moved and handled, during the density measurements, they were extremely fragile. Small chunks were observed falling off various specimens from time to time. This data is rather inaccurate. This might help explain why the control specimens show a higher green density than the 10% glycerol does.

There is a trend among the glycerol samples. As more glycerol is added a higher green density is observed. The 10% glycerol shows an average green density of 49.7%, while 15% glycerol and 20% glycerol new specimens show a green density of approximately 52%. The 20% glycerol old specimens show a green density of 54% and the 25% glycerol old shows a green density of 55%. ‘Glycerol old’ refers to a batch of paste that was sealed in a tub, but sat on the shelf for one week before being cast into test bars. ‘Glycerol new’ refers to a batch of paste that was used within 24 hours of creation.

The freeze-cast bars were then sintered according to the same sintering schedule as all other B<sub>4</sub>C parts (see section 2.2). The density of the sintered parts was also measured via Archimedes’ method with distilled water. The results from these density measurements are shown in Table 3.3.

Table 3.2 Green Densities of Cast Bars with Various Additives

Type of Additive	Average Density (g/cm <sup>3</sup> )	Average Relative Density
10% Glycerol	1.2533 ± 0.0035	0.497 ± 0.001
15% Glycerol	1.3288 ± 0.0143	0.527 ± 0.006
20% Glycerol New	1.3192 ± 0.0033	0.523 ± 0.001
20% Glycerol Old	1.3621 ± 0.0231	0.541 ± 0.023
25% Glycerol New	1.2770 ± 0.0214	0.506 ± 0.009
25% Glycerol Old	1.3976 ± 0.0063	0.554 ± 0.003
Alumina	1.3711 ± 0.2126	0.544 ± 0.085
Aquazol	1.2877 ± 0.0524	0.511 ± 0.021
Control Old	1.3085 ± 0.0281	0.519 ± 0.011
Control New	1.358 ± 0.0103	0.539 ± 0.004
BYK 348	1.1883 ± 0.0035	0.472 ± 0.001
BYK 349	1.1888 ± 0.0090	0.472 ± 0.004

Table 3.3 Sintered Densities of Cast Bars with Various Additives

Type of Additive	Average Density (g/cm <sup>3</sup> )	Average Relative Density
10% Glycerol	2.0690 ± 0.0182	0.821 ± 0.007
15% Glycerol	1.9101 ± 0.1299	0.788 ± 0.051
20% Glycerol New	1.9825 ± 0.0079	0.787 ± 0.003
20% Glycerol Old	2.0160 ± 0.0096	0.800 ± 0.004
25% Glycerol New	2.0080 ± 0.0156	0.797 ± 0.006
25% Glycerol Old	2.1407 ± 0.0086	0.850 ± 0.003
Alumina	1.9415 ± 0.0099	0.770 ± 0.004
Aquazol	1.9598 ± 0.0061	0.778 ± 0.002
Control Old	1.9273 ± 0.0098	0.765 ± 0.004
Control New	1.8959 ± 0.0106	0.752 ± 0.004
BYK 348	1.9166 ± 0.0239	0.761 ± 0.010
BYK 349	1.9161 ± 0.0097	0.760 ± 0.004

As shown in Figure 3.3, the highest average relative sintered density observed is 85.0% from the group marked as 25% glycerol old. The highest density of all the samples is also found in this group with a relative density of 85.4%. The aquazol, alumina, BYK 348, and BYK 349 additives when compared to the control specimens do not show a significant increase in density. This suggests that these additives in the concentrations used are not suitable for ice-crystal size reduction.

**3.3.3. Observation of Ice-crystal Voids.** After the cast bars were finished with post-processing they were mounted onto a metal plate with epoxy and then ground down 1mm with a 200 grit grinding wheel (approximately 75 μm surface finish) to expose the interior. This was done so that the ice crystals could be observed visually under a microscope. Many pictures were taken with the HiRox optical microscope and can be found in Appendix A.

After these bars were observed under the optical microscope they were further polished to 0.25 μm surface finish and observed under a SEM (Hitachi S-570 SEM, Hitachi High-Tech, Japan). These images are in Appendix B. One freeze-cast bar was selected from each additive group to be polished and examined under the SEM.



### 3.4. RESULTS AND DISCUSSION

**3.4.1. Griffith Criterion.** The Griffith criterion can be used to take a known flexural strength and estimate the critical flaw size or to take a known flaw size and estimate a potential flexural strength. With the Griffith criterion there are various situations in which the Y parameter changes. In the particular situation for the printed bars it was assumed that there is a through-thickness internal crack in a finite width body. The Griffith criterion used is [19]

$$K_{IC} = \sigma_f Y c^{1/2} \quad (5)$$

where  $K_{IC}$  is the fracture toughness,  $\sigma_f$  is the flexural strength,  $c$  is the critical flaw size, and  $Y$  depends on the flaw type and is defined as [20]:

$$Y = \left[ \frac{2w}{c} \tan\left(\frac{\pi c}{2w}\right) \right]^{1/2} \quad (6)$$

where  $w$  is the width of the specimen and  $c$  is the same critical flaw size parameter as in Equation (5).

**3.4.2. Ice-crystal Void Size Distribution.** To visually observe the arrangement and distribution of the ice-crystal voids the glycerol bars were mapped under low magnification in Figures 3.5, 3.10, and 3.15. Some of the SEM images are shown to help describe the voids that were observed. The rest of the SEM images are in Appendix B.

The voids were measured using the freehand tool in Image J to outline each individual void from the image. Once outlined Image J gave a resulting area. Image J gave the resulting units as “units”. These “units” were then compared to the scale bar within the picture to obtain a ratio between Image J “units” and  $\mu\text{m}$ . From this ratio the Image J units were converted to  $\mu\text{m}$ .

The void size analyses performed on the 10, 20 and 25 wt% by water bars did not include every void present in the respective cross-sections. Instead, SEM images were taken which were representative of various areas of each bar and the size distribution should be representative of the bar as a whole. Counting every single flaw would be

immensely time consuming. For this study only a portion of the flaws from each bar were measured. The number of voids measured from each bar is in the hundreds.

When looking at the low magnification maps of the bars in Figures 3.5, 3.10, and 3.15 the bottom of the bar in the picture is the bottom of the bar as it was cast. In other words, the bottom of the bar in the picture is the surface of the bar which touched the printing substrate. The top of the bar in the picture was open to the air inside the environmental chamber and the sides of the bar in the picture were in contact with the Teflon mold.

No void sizes could be measured from the 15 wt% by water glycerol group. While some images did show signs of ice-crystal voids not enough voids were present to get a desirable representation of the ice-crystal voids within the bar.

The 10 wt% by water freeze-cast bar shown in Figure 3.11 shows a lot of large ice-crystal voids on the outer edges of the bar and smaller ice-crystal voids in the center which look rather similar in shape and size throughout the middle. The white marks towards the middle of the bar are plastic from a weigh boat which stuck to the bar. There are two large voids in the middle of the bar and one in the upper right corner which are voids caused by freeze casting.



Figure 3.5 50x Zoom Map of Freeze-cast Bar #2 (Table 3.3) from the 10 wt% by Water Glycerol Group

One of the most common void sizes observed in the freeze-cast bar with glycerol amount 10 wt% by water is outlined in green using Image J in Figure 3.6. This area is approximately  $55 \mu\text{m}^2$  and is approximately  $17.5 \mu\text{m}$  at its widest dimension. The area of this void corresponds to the green data point in the chart from Figure 3.8.

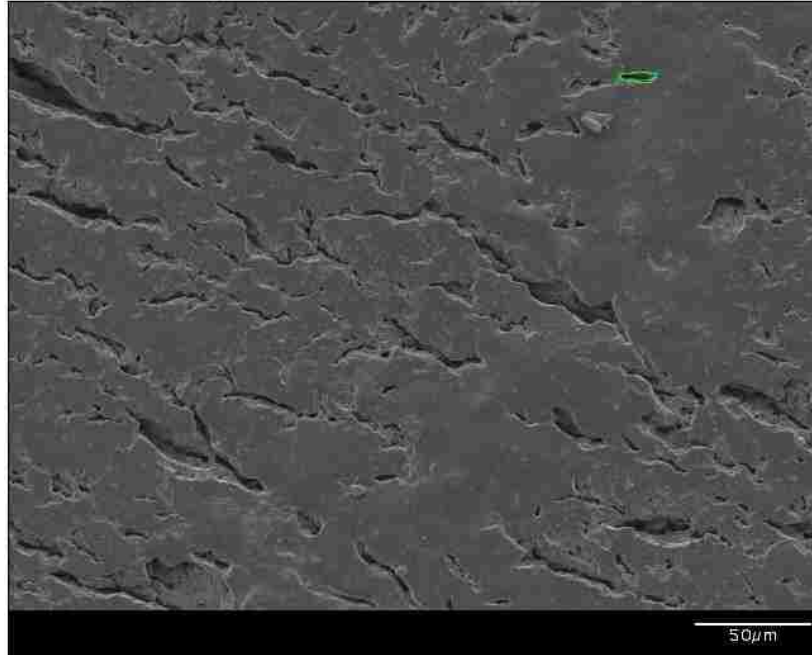


Figure 3.6 SEM Image of 10 wt% by Water Glycerol Bar at 350X Zoom: Green Box from Figure 3.5

One of the largest voids observed is outlined in green in Figure 3.7. It has an area of approximately  $10,500 \mu\text{m}^2$ . The area of this void corresponds to the yellow data point shown in Figure 3.8. Any voids which connected to the border of the bar were ignored for the void measurements.

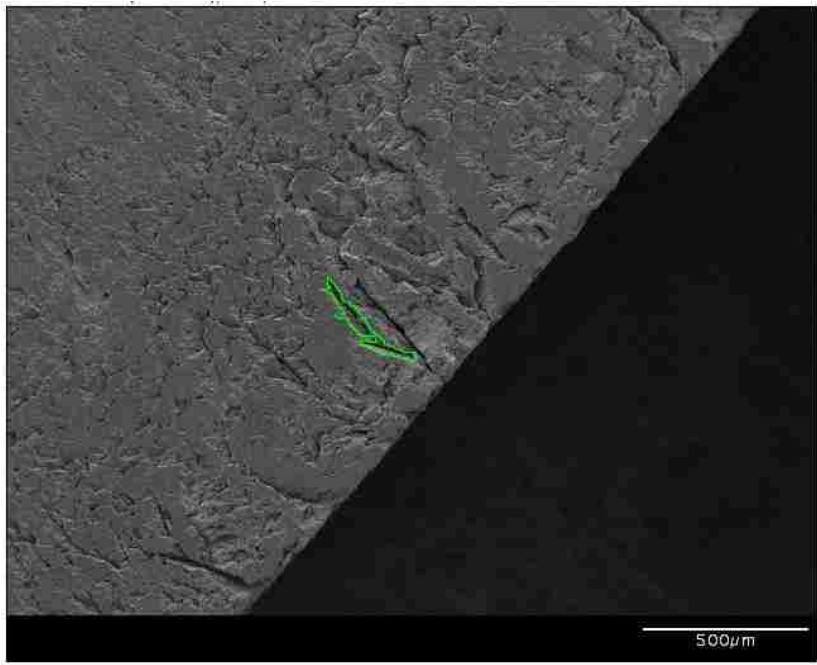


Figure 3.7 SEM Image of 10 wt% by Water Glycerol Bar at 50X Zoom: Yellow Box from Figure 3.5

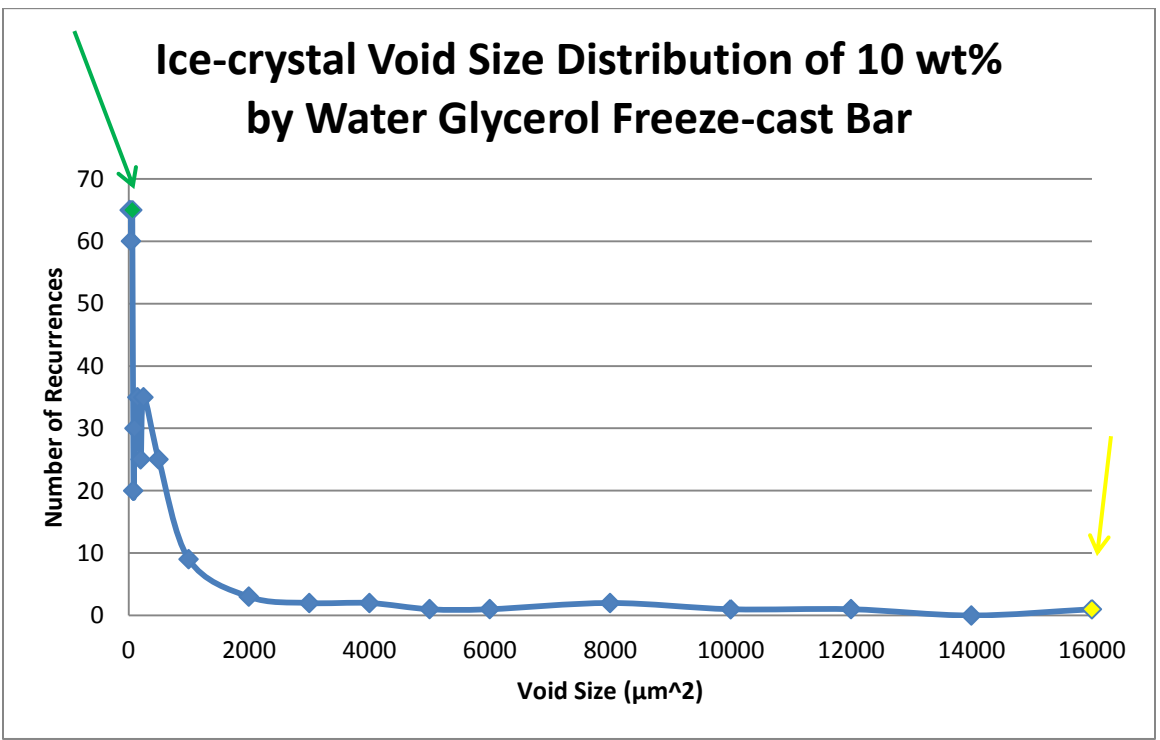


Figure 3.8 Void Size Distribution of 10 wt% by Water Glycerol

Figure 3.8 shows the void size distribution of the 10 wt% by water glycerol freeze-cast bar. In the x-axis the number designated represents any void sizes between it and the previous number. For example, the number of voids observed with a size between 6,000 and 8,000  $\mu\text{m}^2$  is 2 marked under the 8,000  $\mu\text{m}^2$  data point. The same method follows for all other size distribution charts as well.

The void size ranges for this analysis are as follows in table 3.4. These size ranges are the same for the 10, 20 and 25 wt% by water glycerol size analyses.

Table 3.4 Void Size Ranges for Void Size Analysis

Area Range ( $\mu\text{m}^2$ )		
0-20	20-40	40-60
60-80	80-100	100-150
150-200	200-250	250-500
500-1000	1000-2000	2000-3000
3000-4000	4000-5000	5000-6000
6000-8000	8000-10000	10000-12000
12000-14000		

The largest flaw observed in the 10 wt% by water bar was approximately 10,500  $\mu\text{m}^2$  and is represented by the yellow data point in Figure 3.8. The most common void sizes observed were 20-60  $\mu\text{m}^2$  in size. There were between 25 and 35 observed voids in the size groups ranging from 80-500  $\mu\text{m}^2$ . In the group 500-1000  $\mu\text{m}^2$  the number of observations drops to below 10. In this bar there were many more voids observed with an area smaller than 500  $\mu\text{m}^2$  than with a larger area.

The map from Figure 3.5 was used to observe the largest void within the bar that does not touch one of the edges. This void was observed and measured from the low magnification map and was not considered in the void size analysis performed with the SEM images. The sides of the bar were avoided in this search as the sides touching the

Teflon mold most likely experienced freezing conditions that FEF printed bars would not. The largest flaw observed comes from the top left of the bar from Figure 3.5 and is approximately  $0.13 \text{ mm}^2$  ( $130,000 \text{ }\mu\text{m}^2$ ). Its largest width is  $1.508 \text{ mm}$ . It is outlined in green in Figure 3.9. When the Griffith Criterion discussed in section 3.4.1, was used to estimate the flexural strength with a flaw size of  $1508 \text{ }\mu\text{m}$  (c value of  $754\mu\text{m}$ ) the resulting flexural strength was  $70.8 \text{ MPa}$ .

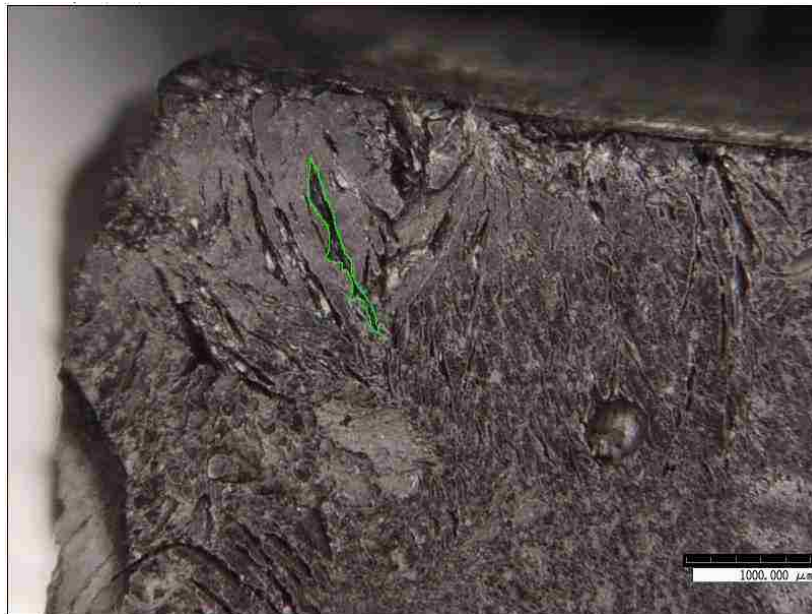


Figure 3.9 Largest Flaw Observed using Optical Microscope in 10 wt% by Water Freeze-cast Bar

The 20 wt% freeze-cast bar shown in Figure 3.10 shows lots of ice-crystal voids of about the same size which appear to be rather evenly spread throughout the bar. Some of the ice-crystal voids at the very top of the bar appear to be larger than those in the middle, but the size difference appears to be much smaller than the 10 wt% by water glycerol freeze-cast bar. The edge effects of the freeze casting do not appear to have affected this bar like they did the 10 wt% by water glycerol bar. There is a very large and

long void or flaw towards the top of the bar. This void was caused during freeze-casting and was ignored during the analysis of the ice-crystal sizes.

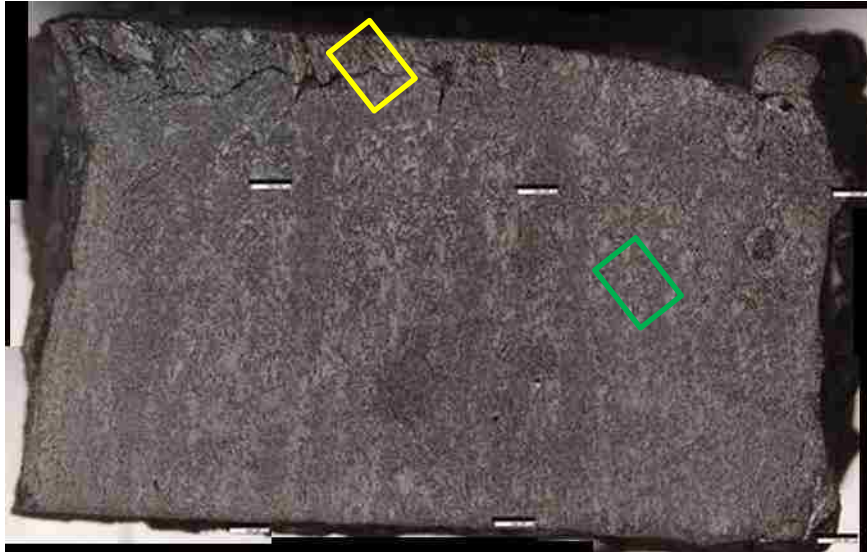


Figure 3.10 50X Zoom Map of Freeze-cast Bar #2 Old (Table 3.3) from the 20 wt% by Water Glycerol Group



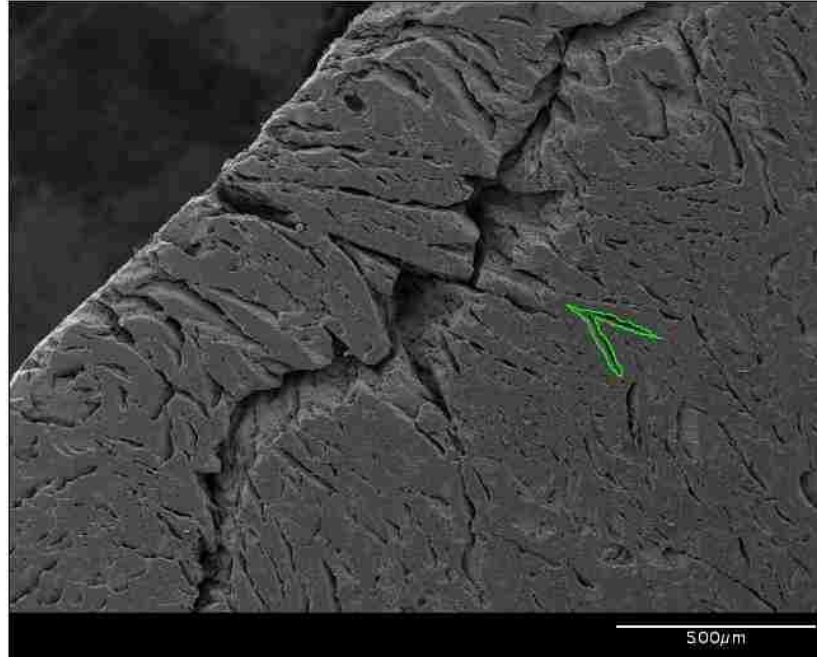


Figure 3.11 SEM Image of 20 wt% by Water Glycerol Freeze-cast Bar at 60X Zoom: Yellow Box from Figure 3.10

Figure 3.11 shows the largest void size observed for the size distribution analysis outlined in green. This void is approximately  $7,000 \mu\text{m}^2$ . The area of this void corresponds to the yellow data point shown in Figure 3.13.

Figure 3.12 shows one of the most commonly observed void sizes in the 20 wt% glycerol bar outlined in green. The void outlined in green is approximately  $680 \mu\text{m}^2$ . This void size is denoted by the green data point in the void size distribution chart shown in Figure 3.13.

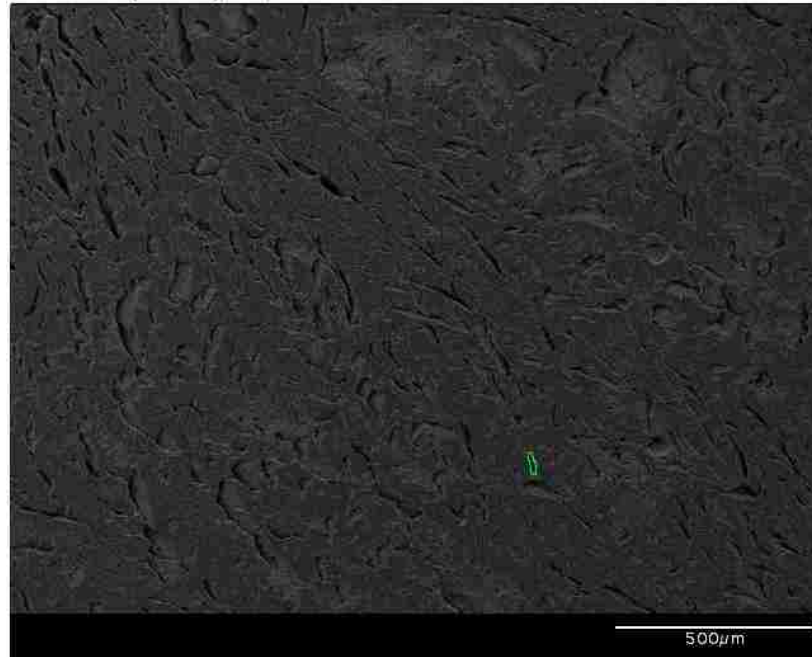


Figure 3.12 SEM Image of 20 wt% by Water Glycerol Bar at 60X Zoom: Green Box from Figure 3.10

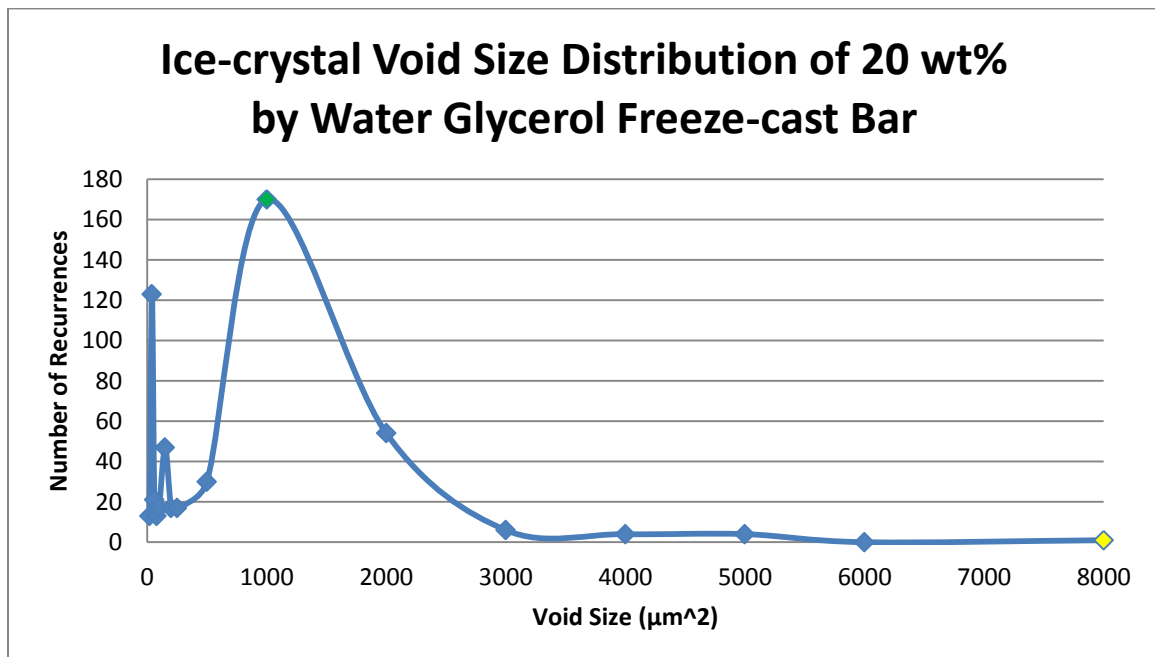


Figure 3.13 Void Size Distribution of 20 wt% by Water Glycerol Freeze-cast Bar

The most common void size observed in the 20 wt% by water freeze-cast bar is  $500 - 1000 \mu\text{m}^2$  and is marked as the green data point in Figure 3.13. The largest flaw observed from the SEM images was  $7,000\mu\text{m}^2$  and is marked as the yellow data point in the same figure. According to the size distribution there were 123 voids in the  $20-40 \mu\text{m}^2$  range. The  $1,000-2,000 \mu\text{m}^2$  size group had just over 60 voids observed. All other groups contain a lower number of void observations. There were 298 voids observed which were smaller than  $500 \mu\text{m}^2$  while there were 239 voids observed which were larger than  $500 \mu\text{m}^2$ .

The map from Figure 3.10 was used to find the largest flaw within the bar that does not touch one of the edges. This void was observed and measured from the low magnification map and was not considered in the void size analysis. The sides of the bar were avoided in this search as the sides touching the Teflon mold most likely experienced freezing conditions that FEF printed bars would not. The void is shown in Figure 3.14 and is outlined in green. This void has an area of approximately  $41,000 \mu\text{m}^2$ . It most likely consists of two individual ice crystals which interconnected with each other while the slurry was freezing. Its largest width is  $465 \mu\text{m}$ . Another void which did not have as large an area had a width of  $542 \mu\text{m}$ . The 20 wt% by water glycerol bar was not flexure-tested, but when the Griffith Criterion discussed in section 3.4.1 is used to estimate its flexural strength with the flaw size of  $542 \mu\text{m}$  (c value of  $271 \mu\text{m}$ ) the resulting flexural strength is  $119.7 \text{ MPa}$ .

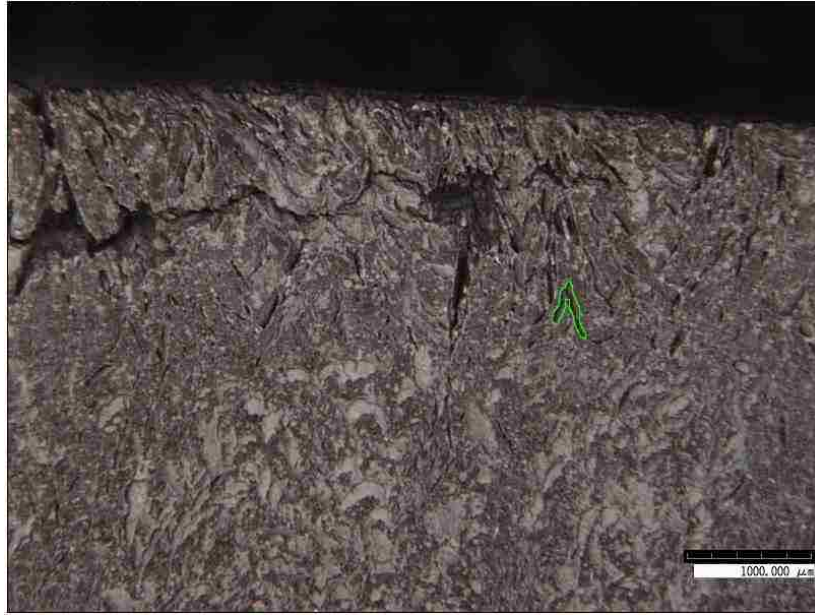


Figure 3.14 Largest Flaw Observed by Optical Microscope in 20 wt% by Water Freeze-cast Bar

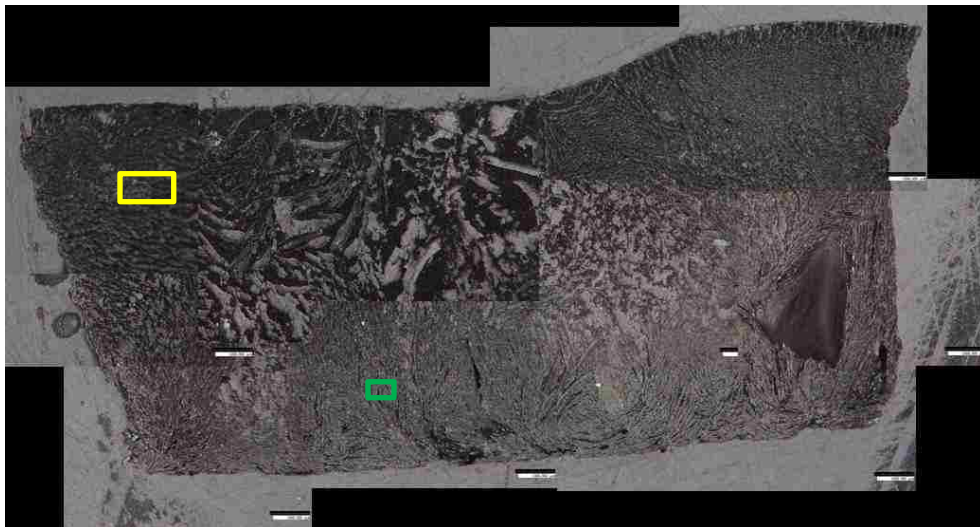


Figure 3.15 50X Zoom Map of Freeze-cast Bar #3 Old (Table 3.3) from the 25 wt% by Water Glycerol Group

In Figure 3.15 it looks like there is some discontinuity between the pictures. This occurs because as the pictures were taken the brightness of the camera was adjusted and the remaining pictures taken turned out brighter than those taken previously.

The 25 wt% by water glycerol freeze-cast bar from Figure 3.15 shows large ice crystal voids spread all throughout the bar. The edge effects do not seem to have affected this bar like the 10 wt% glycerol bar. There does not seem to be any pattern as to where large or small ice crystal voids may occur. There is a rather large void or flaw on the right side of this bar. This was caused during freeze-casting.

One of the largest flaws observed in the SEM images is approximately  $15,700 \mu\text{m}^2$  as shown in Figure 3.16. This void is marked as the yellow data point in Figure 3.18. Many of the voids in this figure appear to have formed because several small ice crystals have interconnected with each other. Some of the voids in Figure 3.16 interconnect with other voids creating several rather large ice-crystal voids.

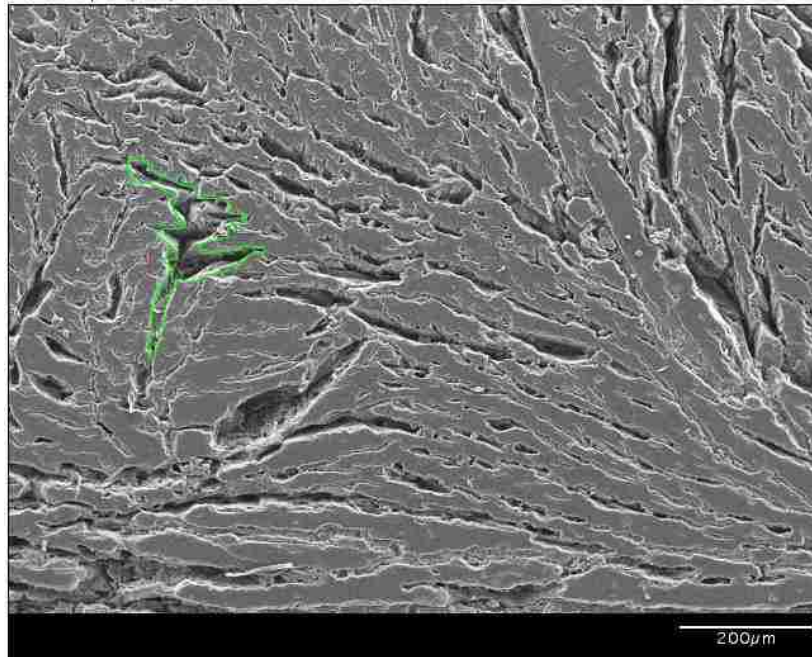


Figure 3.16 SEM Image of 25 wt% by Water Glycerol Bar at 100X Zoom: Yellow Box from Figure 3.15

One of the most common void sizes observed is outlined in green in Figure 3.17. This void has an approximate area of  $440 \mu\text{m}^2$ . This void size is denoted by the green data point in the void size distribution chart shown in Figure 3.18.

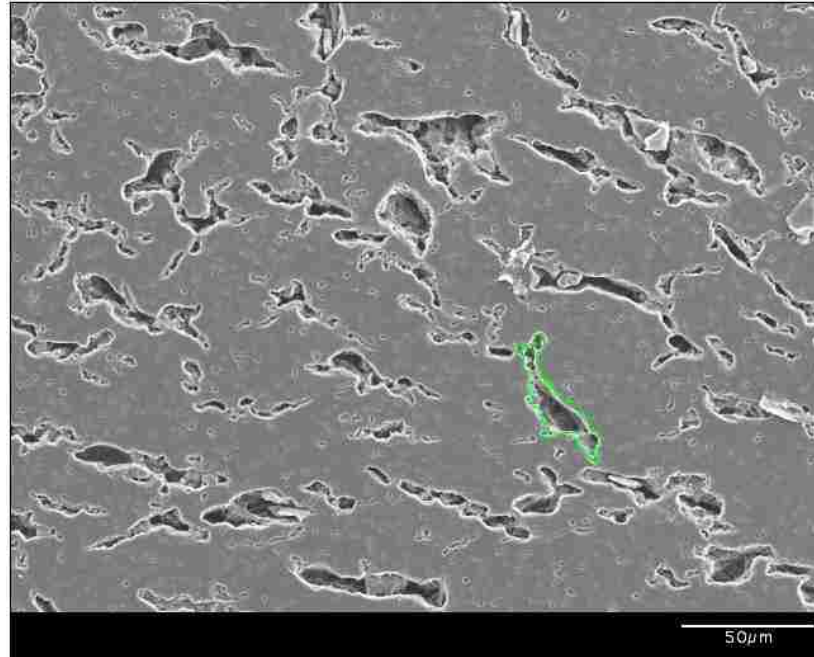


Figure 3.17 SEM Image of 25 wt% by Water Glycerol Barat 400X Zoom: Green Box from Figure 3.15

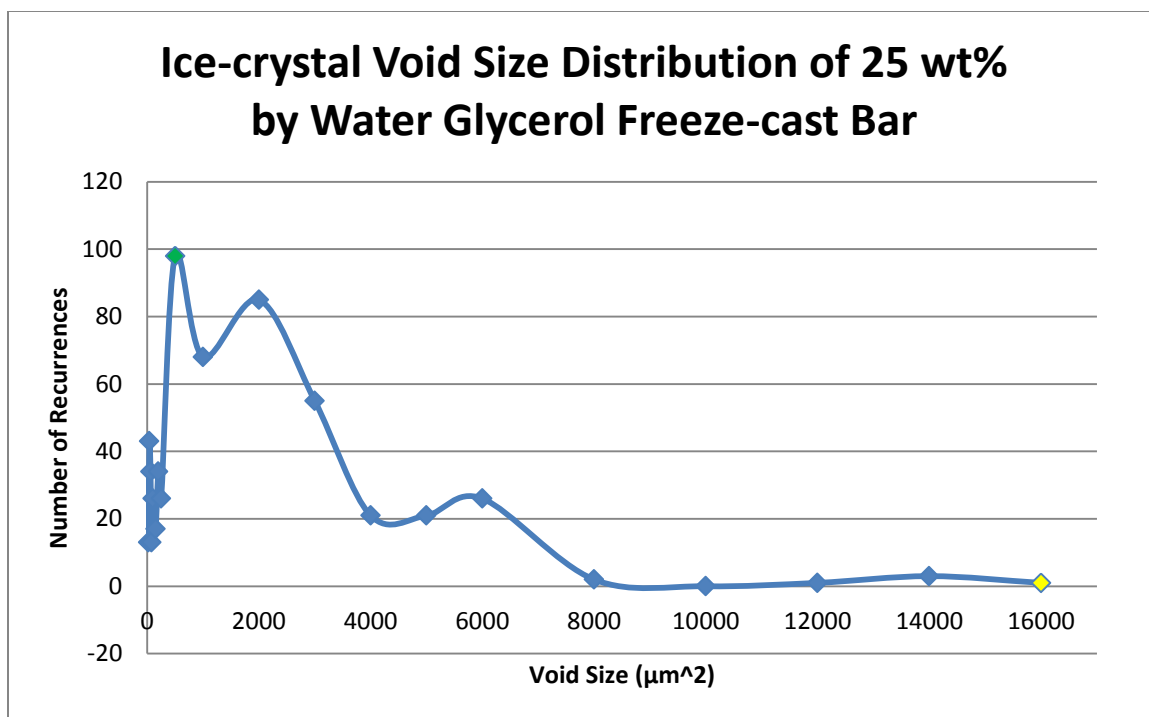


Figure 3.18 Void Size Distribution of 25 wt% by Water Glycerol Freeze-cast Bar

The most common void size observed in the 25 wt% by water glycerol bar was in the size range of 250-500  $\mu\text{m}^2$ . These flaws are marked by the green data point in Figure 3.18. The largest void observed from the SEM images is approximately 15,700  $\mu\text{m}^2$ . This void is marked as the yellow data point in Figure 3.18. The number of small voids (0-250  $\mu\text{m}^2$ ) is rather low compared to the number of large voids. Each size category up to 250  $\mu\text{m}^2$  has between 10 – 45 observed voids. The number of observed voids of a size ranging 500 – 1000  $\mu\text{m}^2$  is 68, while the number of voids ranging from 1000-2000  $\mu\text{m}^2$  is 85. There are many more observed voids larger in size than 500  $\mu\text{m}^2$  than observed voids smaller. When compared to the 50X Zoom map in Figure 3.15 this corresponds. There appear to be lots of large voids spread all throughout the bar.

The 50X zoom map from Figure 3.15 was used to find the largest void within the 25 wt% by water freeze-cast bar that does not touch one of the edges. This void was observed and measured from the low magnification map and was not considered in the

void size analysis. The sides of the bar were avoided in this search as the sides touched the Teflon mold during freeze casting and most likely experienced freezing conditions that FEF printed bars would not. The void is shown in Figure 3.19 and is outlined in green. This largest void has an area of approximately  $0.142 \text{ mm}^2$  ( $142,000 \text{ }\mu\text{m}^2$ ). It most likely consists of a few individual ice crystals which interconnected while the slurry was freezing. Its widest dimension is  $2,171 \text{ }\mu\text{m}$ . This 25 wt% by water glycerol bar was not flexure-tested, but when the Griffith Criterion discussed in section 3.4.1 is used to estimate its flexural strength with the flaw size of  $2,171 \text{ }\mu\text{m}$  (c value of  $1085 \text{ }\mu\text{m}$ ), the resulting flexural strength is  $58.1 \text{ MPa}$ .

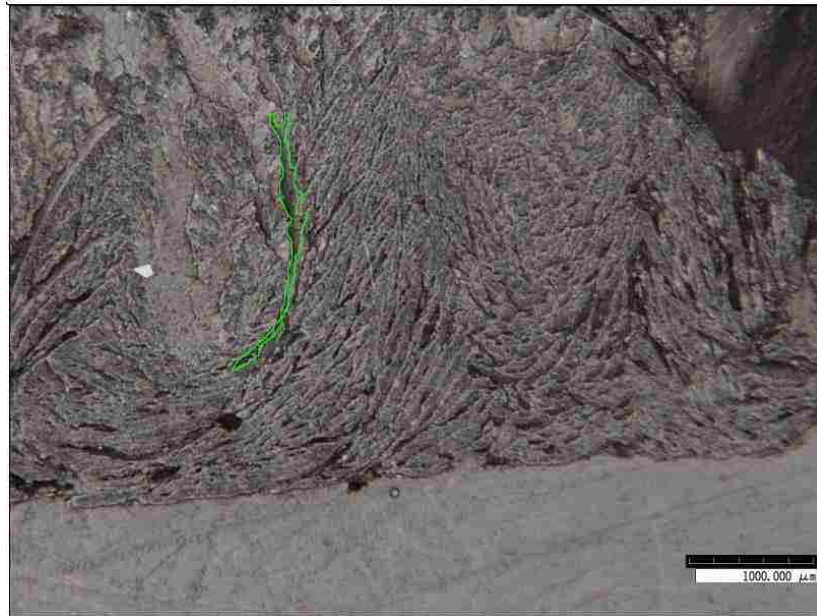


Figure 3.19 Largest Flaw Observed by Optical Microscope in 25 wt% by Water Freeze-cast Bar

Table 3.5 sums up some of the important data from the void size analysis. There do not seem to be any trends as glycerol concentration changes. The 10 wt% by water freeze-cast bar has the smallest most commonly observed void size. The 25 wt% by water



glycerol freeze-cast bar has the largest observed ice-crystal voids from both the SEM (15,700  $\mu\text{m}^2$ ) and optical images (142,000  $\mu\text{m}^2$ ) and had the widest observed void (2171  $\mu\text{m}$ ). The 20 wt% by water glycerol freeze-cast bar had the lowest standard deviation of 1729 and seems to have the most consistent void sizes of the glycerol freeze-cast bars. It also had the lowest observed void sizes from the SEM and optical images and its largest void had the smallest width of 542  $\mu\text{m}$ .

Table 3.5 Comparison of Ice-crystal Voids of Different Glycerol Concentrations

Concentration of Glycerol by Weight of Water	Most Commonly Observed Void Size ( $\mu\text{m}^2$ )	Largest Observed Void Size from SEM ( $\mu\text{m}^2$ )	Largest Void Size from Optical Images ( $\mu\text{m}^2$ )	Longest Width Void Observed from Optical Images ( $\mu\text{m}$ )	Potential Flexural Strength Based on the Griffith criterion (MPa)
10%	55	10500	130000	1508	70.8
15%	N/A	N/A	N/A	N/A	N/A
20%	680	7000	41000	542	119.7
25%	440	15700	142000	2171	58.1

According to Table 3.3 the 10, 20 and 25 wt% by water glycerol freeze-cast bars had a sintered relative density of 81.9%, 79.7% and 85.4% respectively. As shown in Table 3.4, the 20 wt% by water freeze cast bar has the highest potential flexural strength, but it has the lowest sintered relative density of the three being considered.

One possible explanation for this is that the width of 542  $\mu\text{m}$  from Table 3.4 may not actually be the largest void within the bar. There may be larger voids within this bar which do not appear on the particular polished cross-section shown in Figure 3.15. If there are larger voids elsewhere within the bar, these voids would obviously decrease the density of the bar.

**3.4.3. Increasing the Solids Loading.** In the work performed by Sofie and Dogan [15], Figure 3.20 shows how the solids loading of the alumina slurry affects the sintered density. According to Figure 3.21, a solids loading of approximately 50vol% resulted in a sintered relative density of approximately 78%. From the figure, as the solids loading of the slurry goes up, so does the sintered density.

The solids loadings of all freeze-cast B<sub>4</sub>C slurries were approximately 50 vol% ( $\pm 1$  vol%). In Figure 3.21 the resulting sintered relative density of the alumina slurry was about 78%. The resulting densities of all of the B<sub>4</sub>C slurries vary, but the sintered relative density at 50 vol% for the glycerol slurry with a concentration of 25 wt% by water had an average of 85.0%. According to the trend shown in Figure 3.21 if the B<sub>4</sub>C paste or slurry could be made with higher solids loading then better sintered relative density should result.

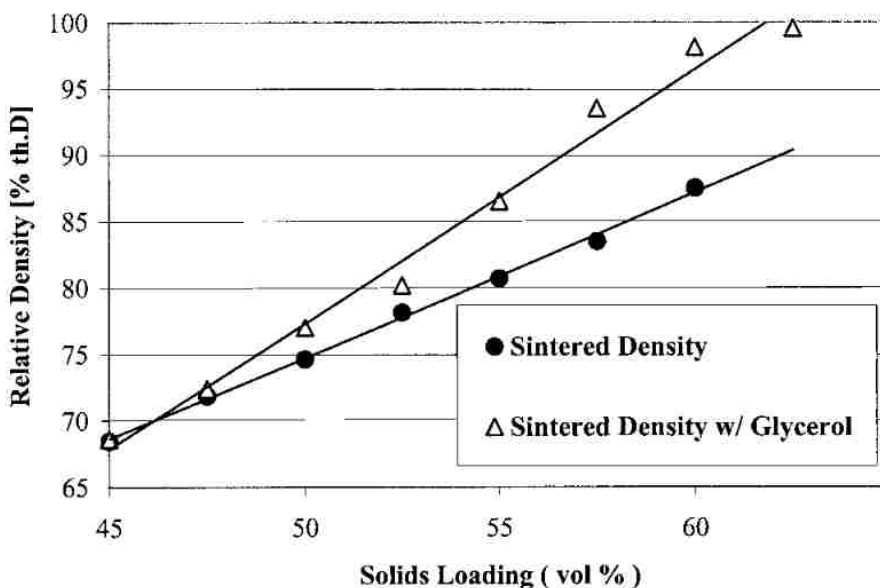


Figure 3.20 Relation Between Solids Loading of Slurry and Relative Sintered Density [15]

Sofie and Dogan [15] went on to further explain that as solids loading increases more particles are packed into the same space. This tighter packing creates more nucleation sites and helps to inhibit ice-crystal growth. They stated that a slurry with a solids loading of 60 vol% or higher could possibly eliminate the freezing structure of the water within the alumina slurry. Thus, if the solids loading of the  $B_4C$  slurry or paste could be increased it could help decrease or eliminate the large ice-crystal voids.

**3.4.4. Comparison of Green and Sintered Relative Densities.** The densities of all of the freeze-cast bars were compared to the iso-pressed powder bars [17] in Figure 3.21. In the figure, the x-axis is the green relative density, and the y-axis is the sintered relative density.

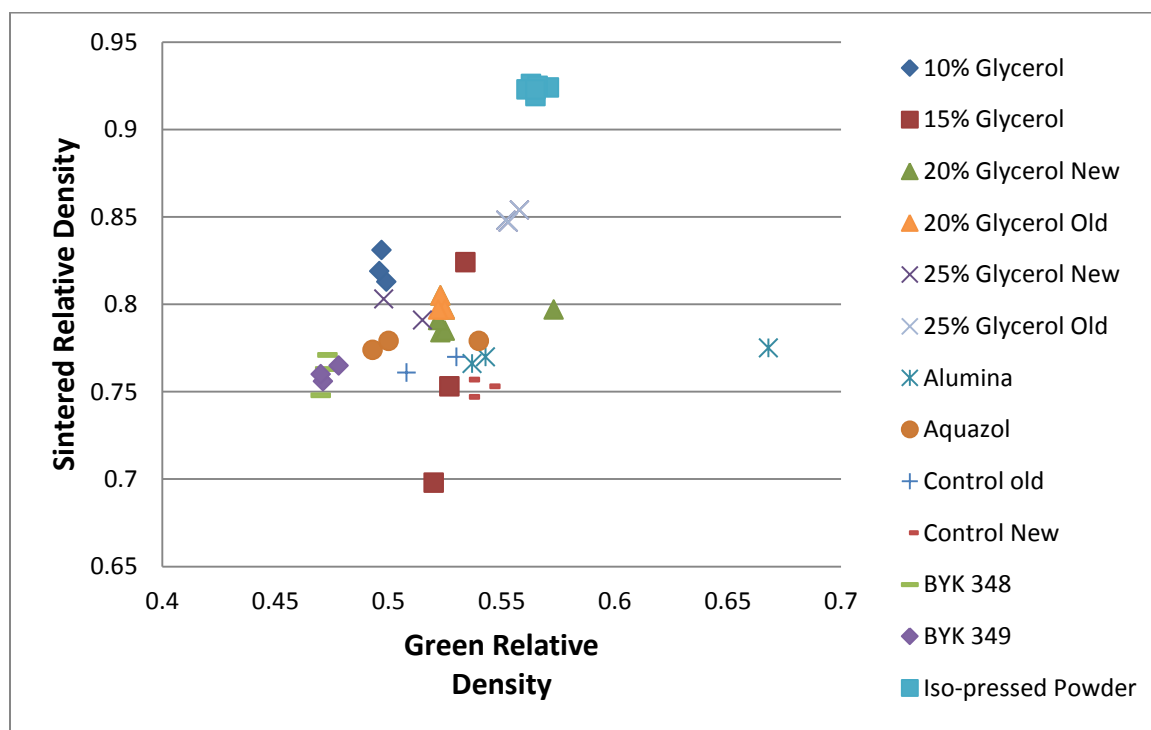


Figure 3.21 Comparison of  $B_4C$  Freeze-Cast Densities to  $B_4C$  Iso-pressed Powder Densities

In Figure 3.21 the green density of many of the freeze-cast bars is about the same as that of the iso-preserved bars (within 5%). However, the iso-preserved bars still have a higher sintered density of 92%, while the highest sintered relative density is among the 25 wt% by water glycerol group of 85.4%. While improving the green density of the freeze cast bars would help improve the sintered density, it is already within the same range as the iso-preserved bars. Since the two green densities are almost the same, ideally the freeze-cast bars should result in a similar sintered density as the iso-preserved bars. Since they do not exhibit similar densities, this means that in reality the ice-crystal voids were within the freeze-cast bars in the green state. The significant difference in sintered density is because of the presence of the large ice-crystal voids. When the ice crystals form they act like bulldozers and push the powder packing it between ice-crystal voids. When the ice is freeze-dried, the water leaves a large void which cannot be filled during sintering.

Sintered relative density vs. green relative density of the glycerol specimens was plotted with the data from the iso-preserved bars in order to better visually see if there is a trend as glycerol concentration changes. Figure 3.22 shows this comparison.

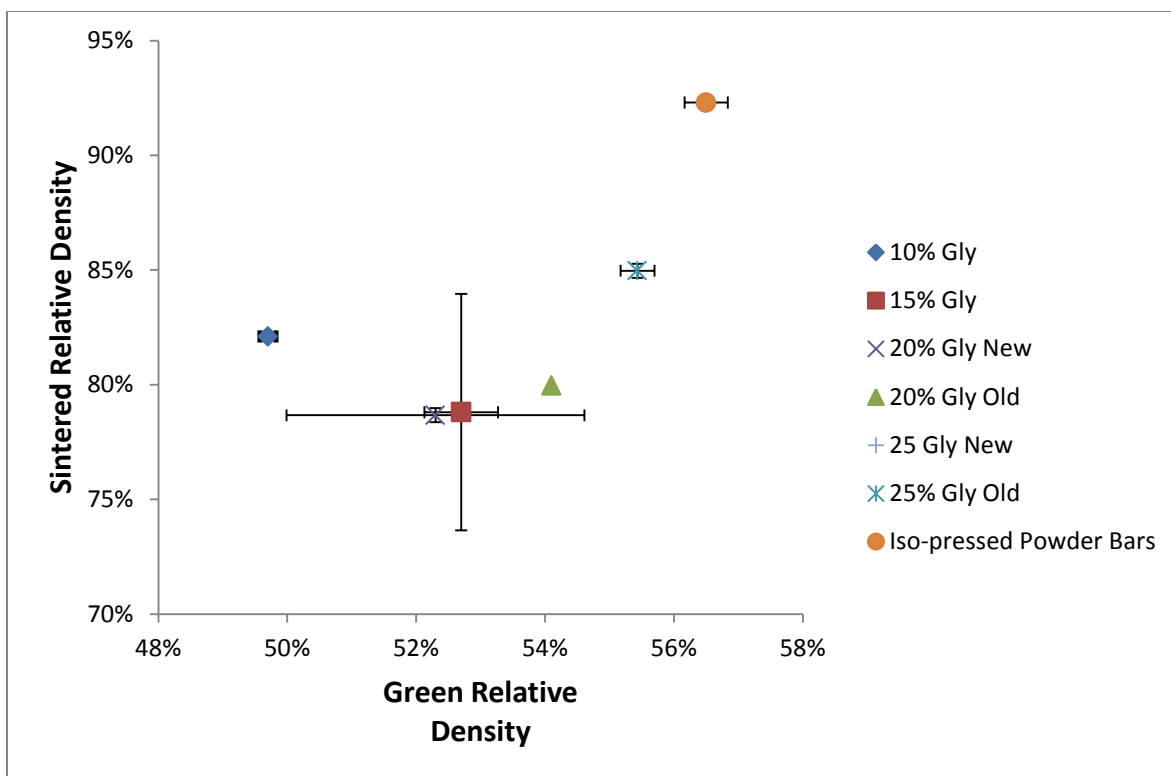


Figure 3.22 Comparison of B<sub>4</sub>C Densities with Glycerol Concentration to B<sub>4</sub>C Iso-pressed Bars

The error bars included in the figure are the standard deviations. As seen in Figure 3.22 the average densities do not seem to follow any trend. Therefore, no definite trend can be interpolated about a relation between glycerol concentration and change in density.

The large error bars seen in some of the green densities can be attributed to large standard deviations in the green density. This large variation in the data was caused by the way the green density was measured. During the measurements physical manipulation of the fragile green parts caused small pieces of material to fall off of some of the specimens. This material falling off would cause results to be reported that do not reflect the true green density. As can be seen in Figure 3.21, one of the alumina specimens has a green relative density of over 65%. This should be in error as the solids loading of the alumina additive slurry was about 50vol%.

### 3.5. TEST BARS FABRICATED BY THE FEF PROCESS WITH ADDITIVE

The slurry with a glycerol content of 25 wt% by water was chosen to be used to print bars. It was desired to compare the density and flexure strength of these bars with those printed without additives. Table 3.6 shows the results of the bars printed with glycerol as an additive with a concentration of 25 wt% by water.

Table 3.6 Flexural Strength and Densities of FEF Printed Bars with a Glycerol Concentration of 25 wt% by Water

Specimen	Maximum Flexure Stress (MPa)	Maximum Flexure Load (N)	Relative Density
1	61.0	74.4	0.834
2	54.5	65.8	0.863
3*	N/A	N/A	0.854
4	62.1	76.7	0.872
5	92.1	110.3	0.840
Average	67.4	81.8	0.853
Standard Deviation	14.5	19.6	0.014

\* This bar broke during loading onto the flexure test fixture and no flexural strength was recorded.

The average relative density of these bars was 85%, which is slightly higher than the 83% relative density resulting from the same slurry which was cast. The average flexure strength was 67.4 MPa which is an increase of 9.2 MPa from the bars printed without any additives (Table 2.2). Another interesting note is that the addition of the glycerol has reduced the standard deviation from 23 in Table 2.2 to 14.5 in Table 3.6. This suggests that the glycerol helps to produce more consistent results.

The average flexure strength is still much lower than desired especially when compared with the iso-pressed powder bars from Table 2.2 which has a mean flexure strength of 255.2 MPa.

After these bars were flexure-tested, the fracture surface was observed under low magnification on the HiRox optical microscope. Figure 3.23 shows two of these pictures.

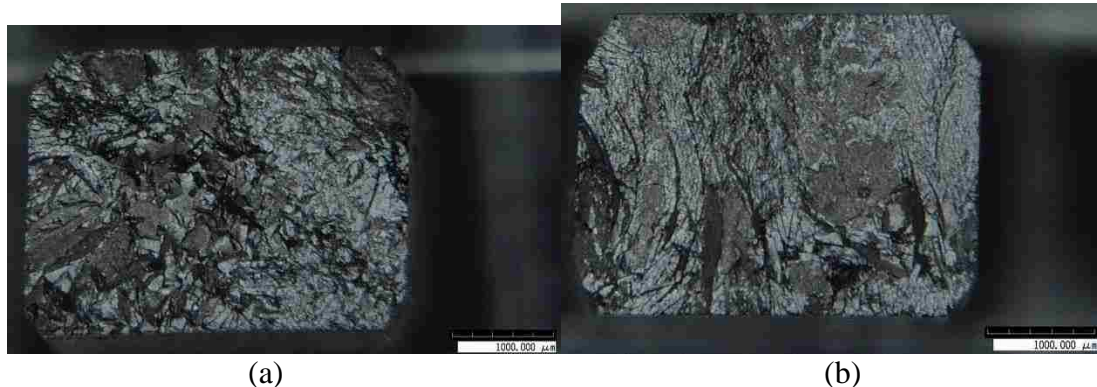


Figure 3.23 Fracture Surfaces of Flexure Test Bars Printed with 25 wt% by Water Glycerol Concentration; (a) Bar #1; (b) Bar #2 from Table 3.6

Like the fracture surfaces shown in Figure 2.12, these bars do not show any flaws due to printing. This suggests that the process parameters used to print them are appropriate.

After plugging the value for  $Y$  from Equation (6) into Equation (5) of the Griffith Criterion in Equation (5), the equation was solved in terms of  $c$ . The fracture toughness ( $K_{IC}$ ) was assumed to be  $3.5 \text{ MPa}\cdot\text{m}^{1/2}$  [1] and the average flexural strength of  $67.4 \text{ MPa}$  from the bars was used for  $\sigma_f$ . Solving for  $c$  gives a value of  $827 \mu\text{m}$ . If the  $Y$  parameter is set to  $\pi^{1/2}$  the resulting  $c$  value is  $858 \mu\text{m}$ . Varying the  $Y$  parameter does not have a large effect on the resulting value of  $c$ . According to the assumption used for the value of  $Y$ , this value is actually half of the critical flaw size. Therefore the actual critical flaw is  $1.6 \text{ mm}$ . This value may seem very large for the size of the bars used, but when it is compared to the widest observed void from the 25 wt% by water glycerol freeze-cast bar ( $2,171 \mu\text{m}$ ), as shown in Figure 3.19, this value is reasonable.

When the Griffith criterion is used to calculate the critical flaw size of the iso-pressed powder bars from Table 2.2, with the same value of the Y parameter, the resulting value of  $c$  is  $60\mu\text{m}$ . This means a flaw size of  $120\ \mu\text{m}$ .

The data from Table 3.4 shows that the potential flexural strength for the 25 wt% by water glycerol bars is 58.1 MPa while Table 3.6 shows a real flexural strength of 67.4 MPa. The potential strength calculated in Table 3.4 only represents what the flexural strength could be if the flaw is perpendicular to the direction of load. This suggests that the flaws within the 25 wt% by water glycerol bars (reflected in Table 3.6) are not lining up perpendicular to the load direction. If these flaws, the ice-crystal voids, are lining up slightly askew to the load direction, then the flaw size would not be the same as the full width of the flaw. It would only be the width of that flaw perpendicular to the load direction.



#### 4. SUMMARY AND CONCLUSION

The process parameters of the FEF machine were calibrated in such a way as to produce flexure test bars free of printed flaws. An appropriate table speed, standoff distance, ram speed, and raster spacing were found. Furthermore, important issues were identified about the process, such as the nozzle alignment and the temperature of the substrate, which have greatly improved the quality and repeatability of parts fabricated from the FEF process.

Despite all of the additives used in this study, large ice-crystal voids could not be eliminated from the test specimens fabricated by the FEF process. The void size analysis revealed that the largest ice-crystal void was observed in the 25 wt% by water glycerol freeze-cast bar. It had an area of  $142,000 \mu\text{m}^2$  and the largest width of  $2,171 \mu\text{m}$ . Glycerol was the only additive that showed an improvement in the sintered relative density, from 76.5% in the control freeze-cast bars to 85.0% in the 25wt% by water glycerol freeze-cast bar. A glycerol concentration of 25 wt% by water was the highest concentration used.

The glycerol paste with 25 wt% by water was almost too thick to be extruded with the FEF process. The maximum extrusion force for the FEF machine used in this study was 1000N, and the 25 wt% by water glycerol paste had a steady state extrusion force of 800 N. Increasing the glycerol concentration would increase the viscosity of the paste so much that it would not be extrudable. Also, increasing the glycerol concentration decreases the required freezing point of the mixed water-glycerol combination [21]. If the glycerol concentration is increased too much, it may not be feasible to freeze the liquid within the paste using the FEF process. Additionally, parts fabricated with a 25 wt% by water glycerol concentration were difficult to handle in the green state. These parts were not solid and rigid like most green parts from the FEF process are. They were sticky to the touch and easily deformable. It would be difficult to handle such green parts without deforming or damaging them in undesirable ways. Increasing the glycerol concentration beyond 25 wt% by water would not be feasible with the FEF process.

The addition of glycerol in a concentration of 25 wt% by water to the paste increased the flexural strength from 58.1 MPa (Table 2.2) to 67.4 MPa (Table 3.6). The

density increased from 76.2% to 85.0%. The addition of the glycerol decreased the standard deviation of the flexural strength from 23.0 to 14.5 MPa. However, the improvements made by adding the glycerol to the paste have not increased the properties to a desired level since bars fabricated from iso-pressed powder resulted in a flexural strength of 255.2 MPa and a density of 88.4% (Table 2.3).

In order for boron carbide to be successful with the FEF process a much better understanding of the surface chemistry of the powder being used is required. Surface energy is most likely not the issue since the contact angle is relatively low at  $40.2^\circ$  (Table 3.1).

The green densities of most of the test slurry specimens used in the FEF process are approximately the same as the iso-pressed powder bars (Figure 3.22). Increasing the solids loading should help increase the sintered relative density and should help reduce the size of the ice-crystal voids but may not be able to fully resolve the issue. In order to obtain specimens with high sintered relative density (>92%) the ice-crystal voids must be eliminated or at least significantly reduced in size and number. According to the Griffith criterion the maximum flaw size should be no larger than 120  $\mu\text{m}$  in order to obtain a flexural strength similar to that obtained from the iso-pressed powder bars. This means that the largest ice-crystal void present in the test bars after fabrication and post-processing should be no larger than 120  $\mu\text{m}$  in the direction perpendicular to the tensile surface.

## 5. FUTURE WORK

Further investigation of the boron carbide surface chemistry could reveal important information about how ice is nucleating onto it. Understanding how the ice nucleates onto this particular powder could lead to solutions that prevent large ice-crystal voids from forming. If ice-crystal voids are to be removed from any material with the FEF process, then knowledge of the surface chemistry is needed. A few issues that could be investigated are; the shape of the boron carbide particles, contaminants present in the powder, the possible presence of borate on the particles after the powder is washed in methanol, the composition of the surface of a typical particle in the powder, the change in surface charge after the powder is dispersed in water (if any), and the efficiency of TMAH covering powder particles properly.

Selecting another powder with a larger particle size and smaller surface area per unit mass could make the dispersion of the boron carbide powder easier. Easier dispersion of particles could lead to increased solids loadings. A different type of powder may contain different types of particles which may nucleate more efficiently than the HD 20 grade powder currently used.

In the future, when developing a new material for the FEF process, it should be freeze cast before printed to better understand how it behaves and how it post-processes. If this had been done with this project, much more time could have been devoted to understanding ice-crystal nucleation on the powder instead of so much time dedicated to the printing of test bars.

Ice-crystal voids have been a problem for a while with the FEF process. It would be worthwhile looking into alternatives to using ice as a binder (using coconut oil, alcohols, drying instead of freezing, etc.).

Since it was observed that the ice crystals are interconnecting with each other and forming long chains of voids it would be worth studying this phenomenon. If the ice crystals could at least be prevented from connecting with each other, then the density and strength of the test bars would increase considerably.

APPENDIX A.

LOW MAGNIFICATION IMAGES (50X ZOOM) OF FREEZE-CAST BARS

All bar numbers correspond to Table 3.3.

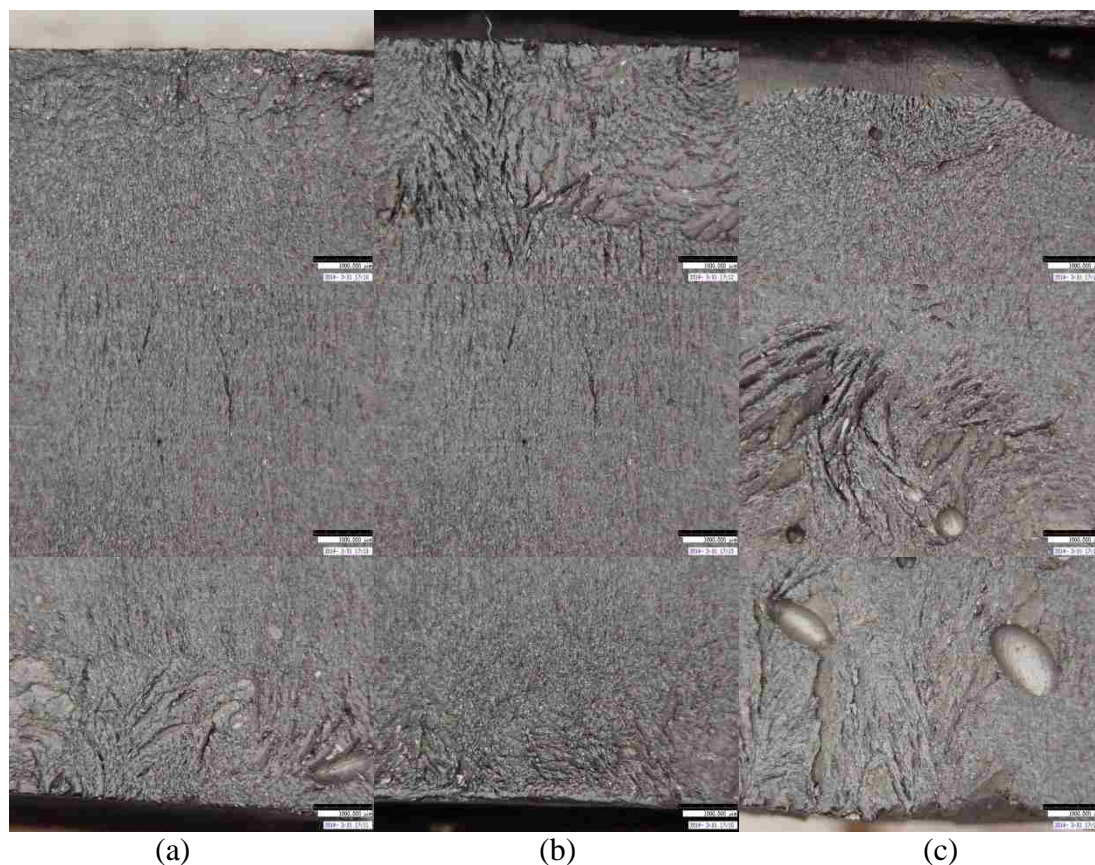


Figure A.1: View of Ice-crystal Voids of Freeze-Cast Bars with a Glycerol Concentration of 10 wt% by Water: (a) Bar #1; (b) Bar #2; (c) Bar #3

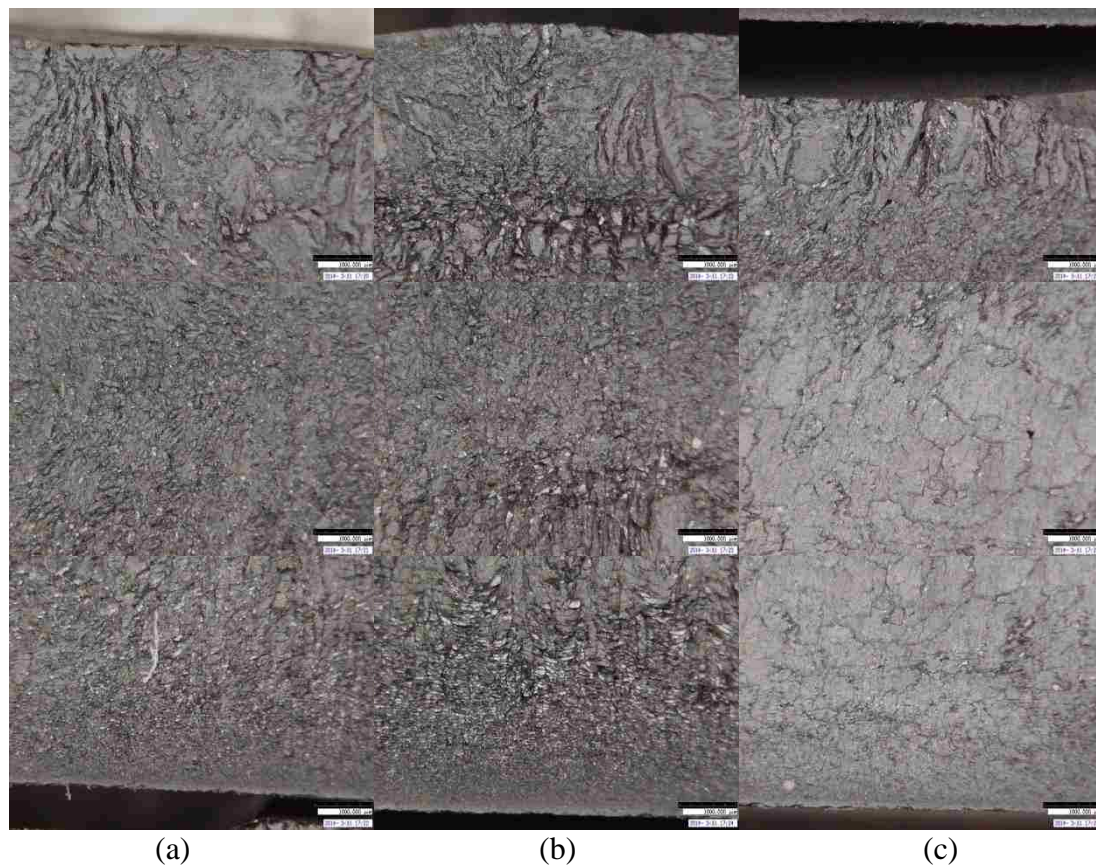
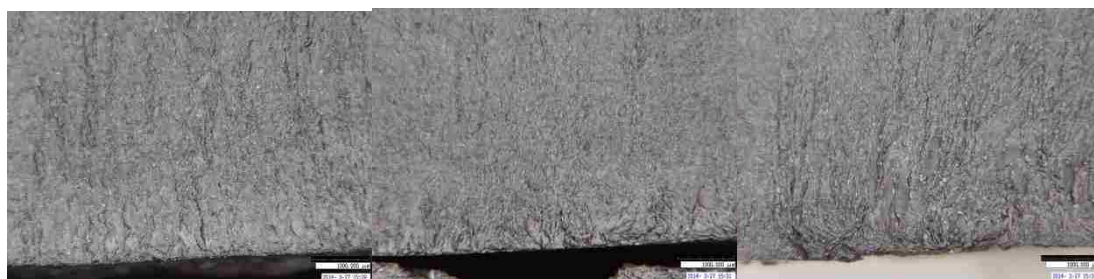
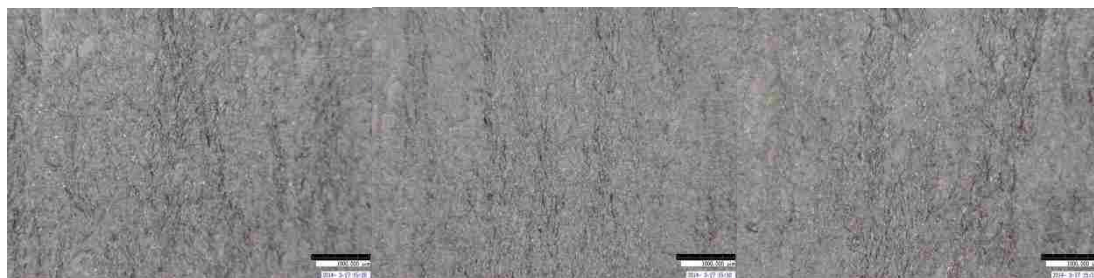
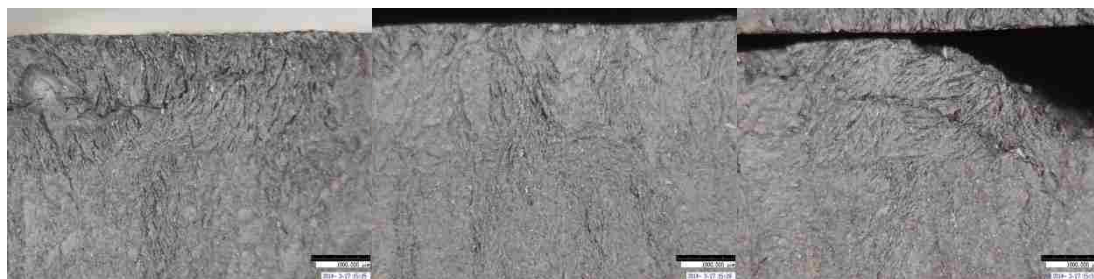


Figure A.2: View of Ice-crystal Voids of Freeze-Cast Bars with a Glycerol Concentration of 15 wt% by Water: (a) Bar #1; (b) Bar #2; (c) Bar #3



(a)

(b)

(c)

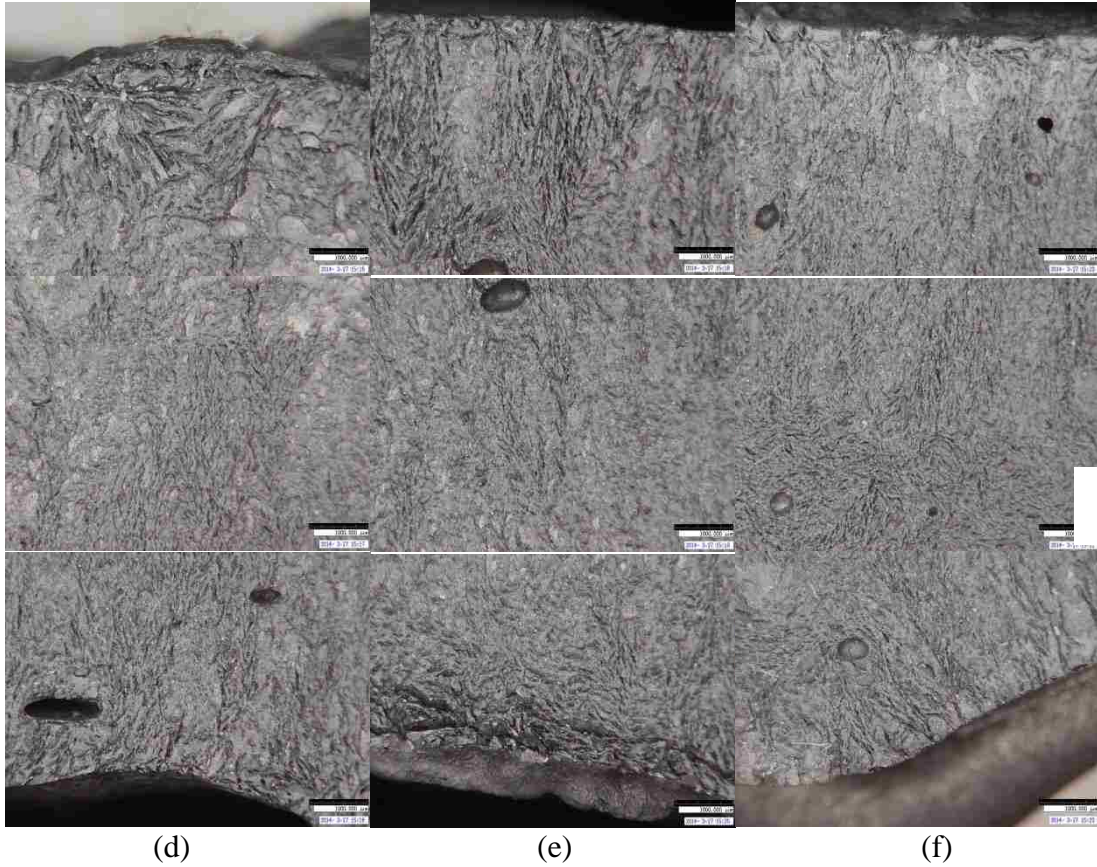
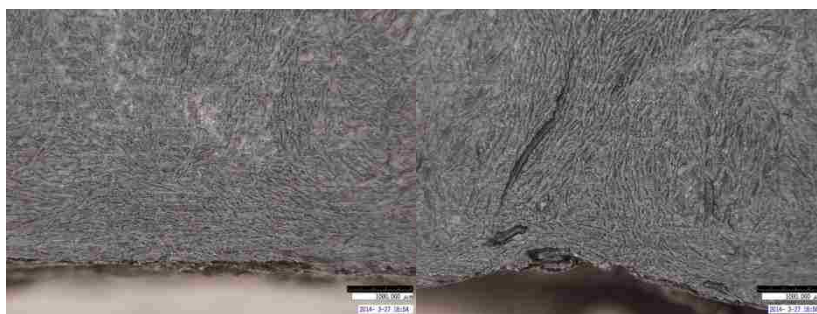
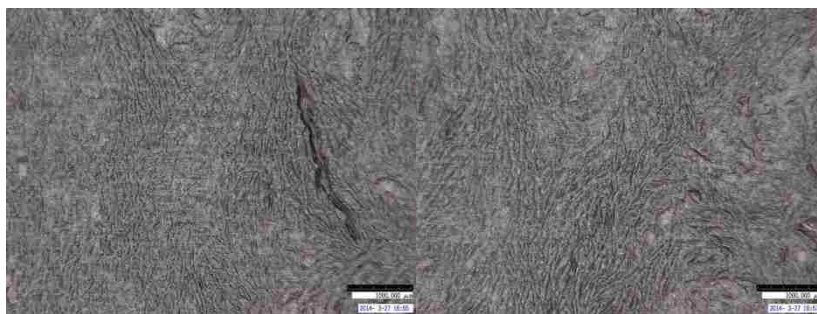
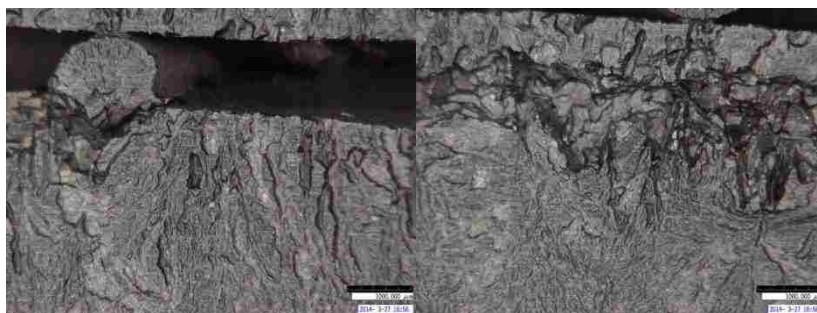


Figure A.3: View of Ice-crystal Voids of Freeze-Cast Bars with a Glycerol Concentration of 20 wt% by Water: (a) Bar #1; (b) Bar #2; (c) Bar #3; (d) Bar #4; (e) Bar #5; (f) Bar #6





(a)

(b)

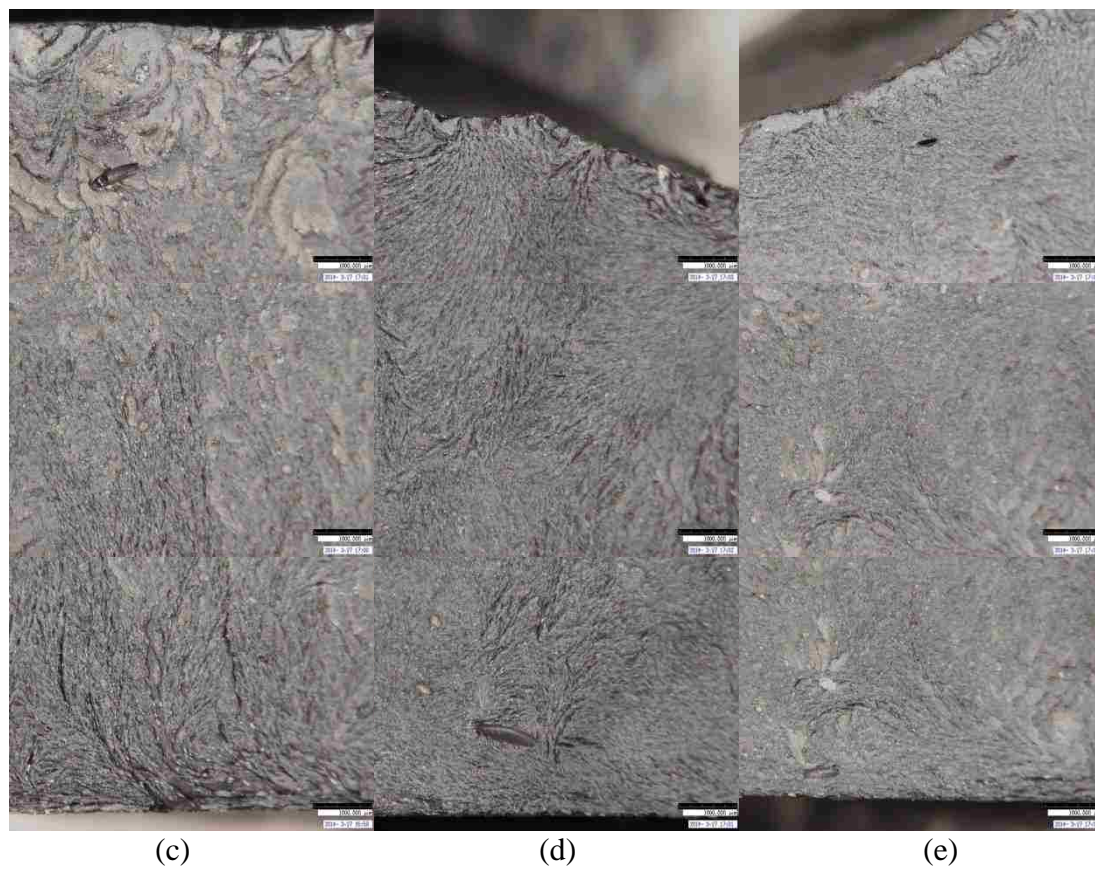


Figure A.4: View of Ice-crystal Voids of Freeze-Cast Bars with a Glycerol Concentration of 25 wt% by Water: (a) Bar #1 New; (b) Bar #2 New; (c) Bar #1 Old; (d) Bar #2 Old; (e) Bar #3 Old;

APPENDIX B.

SEM IMAGES OF FREEZE-CAST BARS

All bar numbers correspond to Table 3.3.

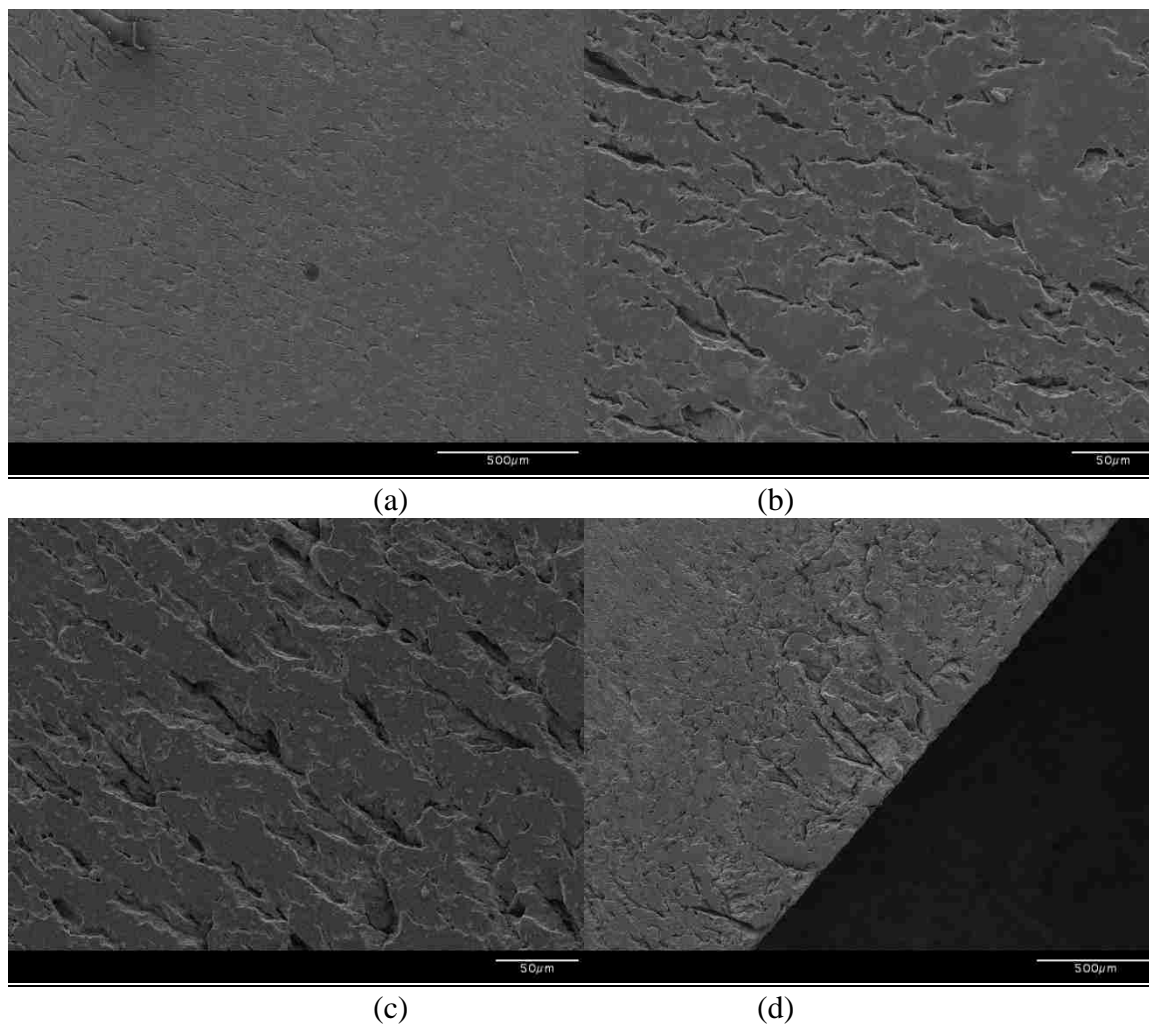
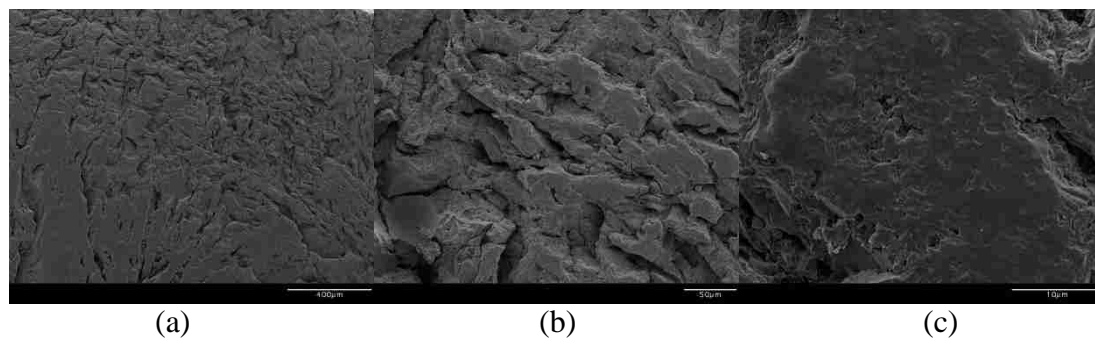


Figure B.1: SEM Images of Freeze-Cast Bar #2 with a Glycerol Concentration of 10 wt% by Water: (a) 60X Zoom; (b) 350X Zoom; (c) 350X Zoom; (d) 50X Zoom



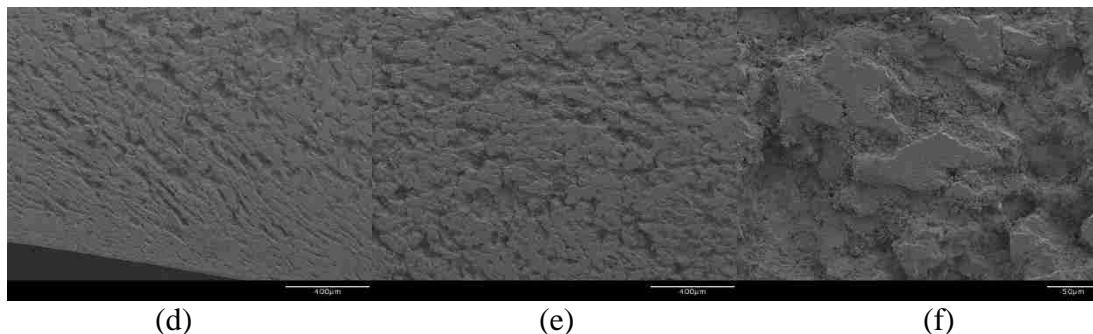


Figure B.2: SEM Images of Freeze-Cast Bar #3 with a Glycerol Concentration of 15 wt% by Water: (a) 70X Zoom; (b) 350X Zoom; (c) 3000X Zoom; (d) 70X Zoom; (e) 70X Zoom; (f) 350X Zoom

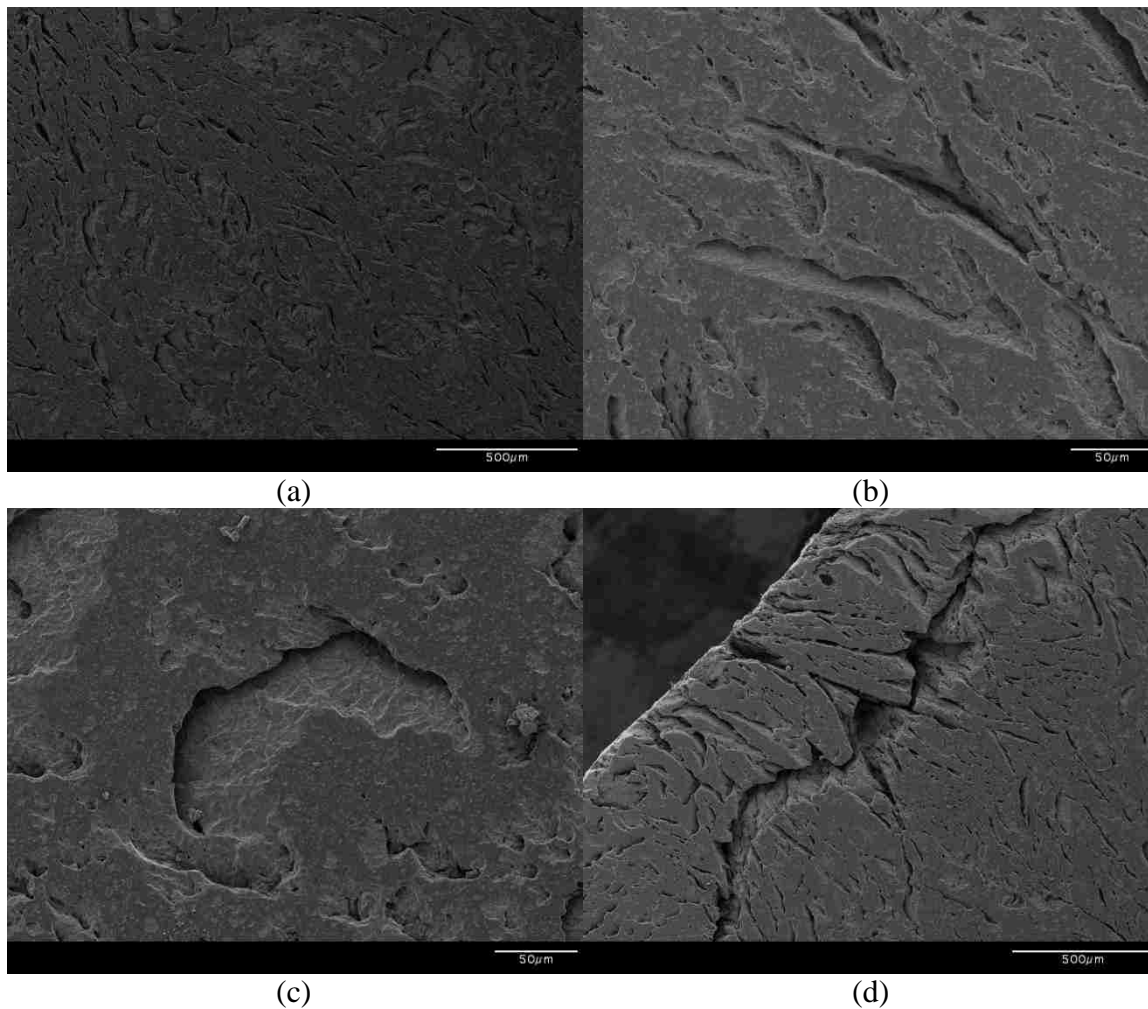


Figure B.3: SEM Images of Freeze-Cast Bar #2 with a Glycerol Concentration of 20 wt% by Water: (a) 60X Zoom; (b) 350X Zoom; (c) 350X Zoom; (d) 60X Zoom

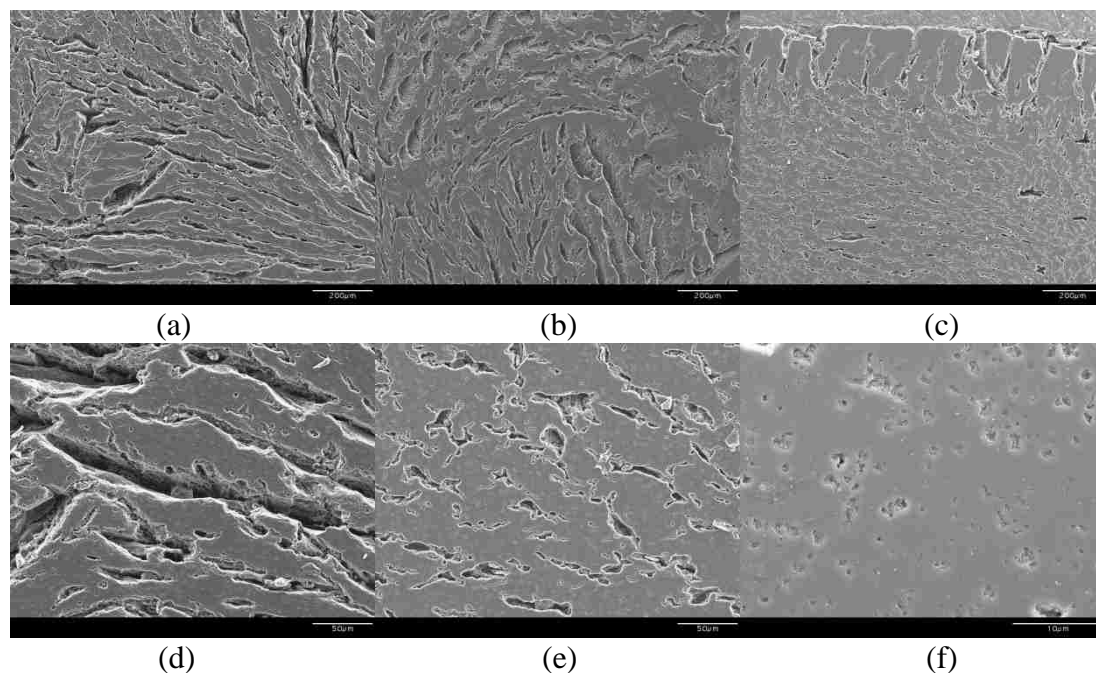


Figure B.4: SEM Images of Freeze-Cast Bar #3 with a Glycerol Concentration of 25 wt% by Water: (a) 100X Zoom; (b) 100X Zoom; (c) 100X Zoom; (d) 400X Zoom; (e) 400X Zoom; (f) 3000X Zoom

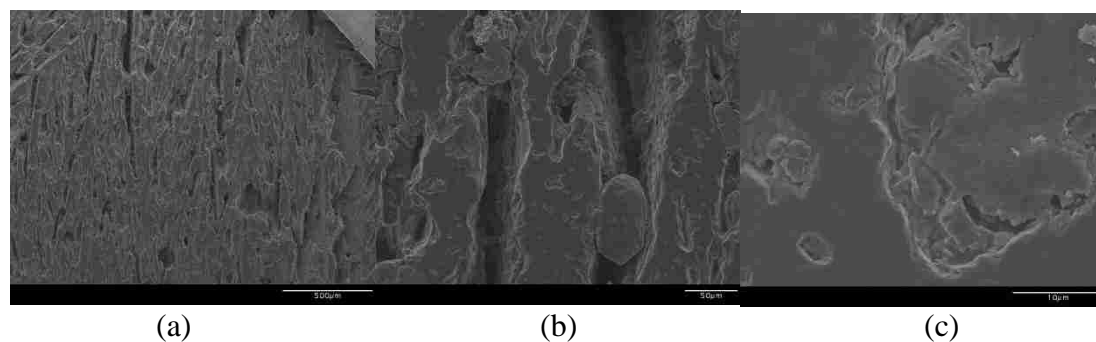


Figure B.5: SEM Images of Freeze-Cast Bar #2 of the BYK 348 Additive Group: (a) 60X Zoom; (b) 350X Zoom; (c) 3000X Zoom;

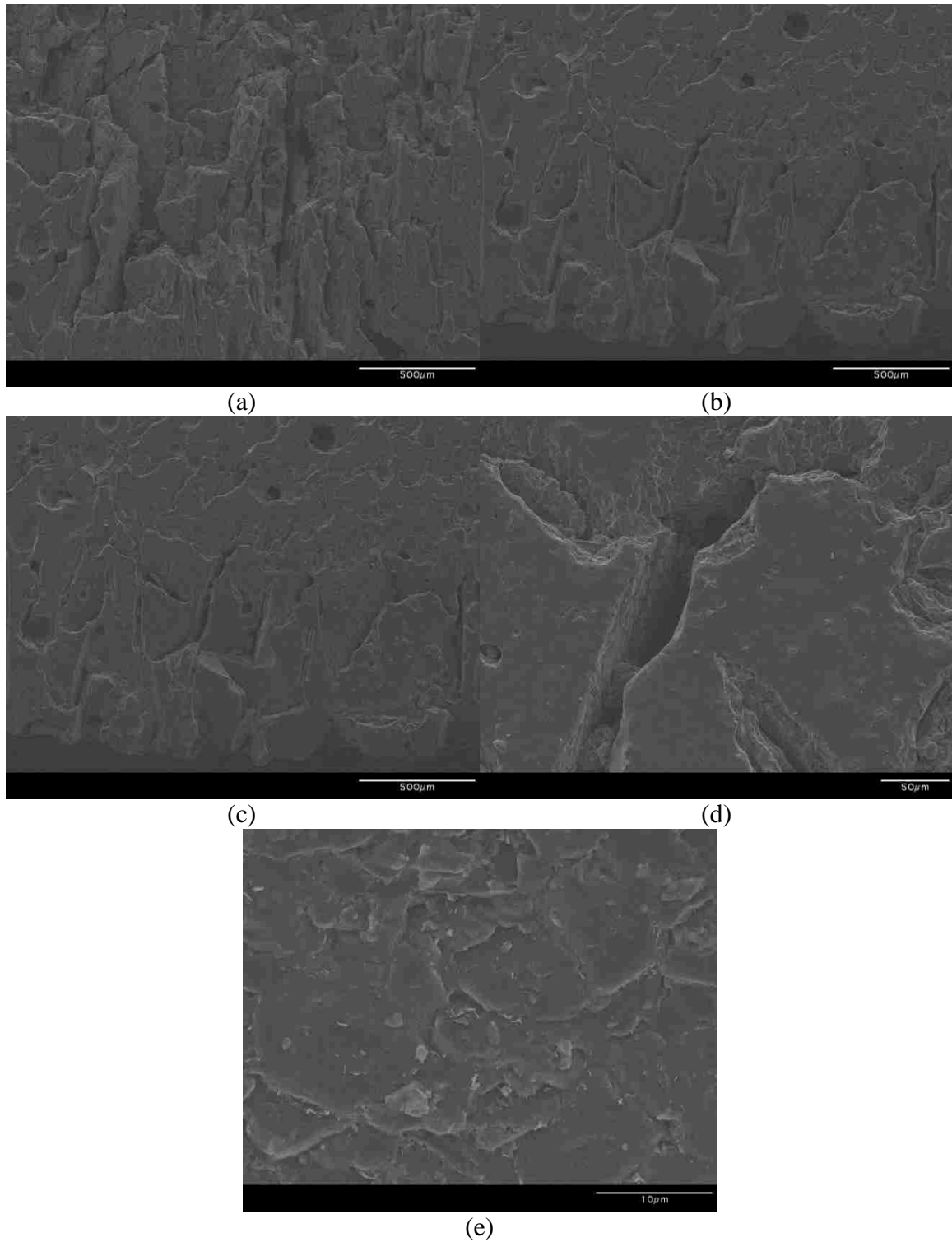


Figure B.6: SEM Images of Freeze-Cast Bar #3 of the BYK 349 Additive Group: (a) 60X Zoom; (b) 60X Zoom; (c) 60X Zoom; (d) 350X Zoom; (e) 3000X Zoom;

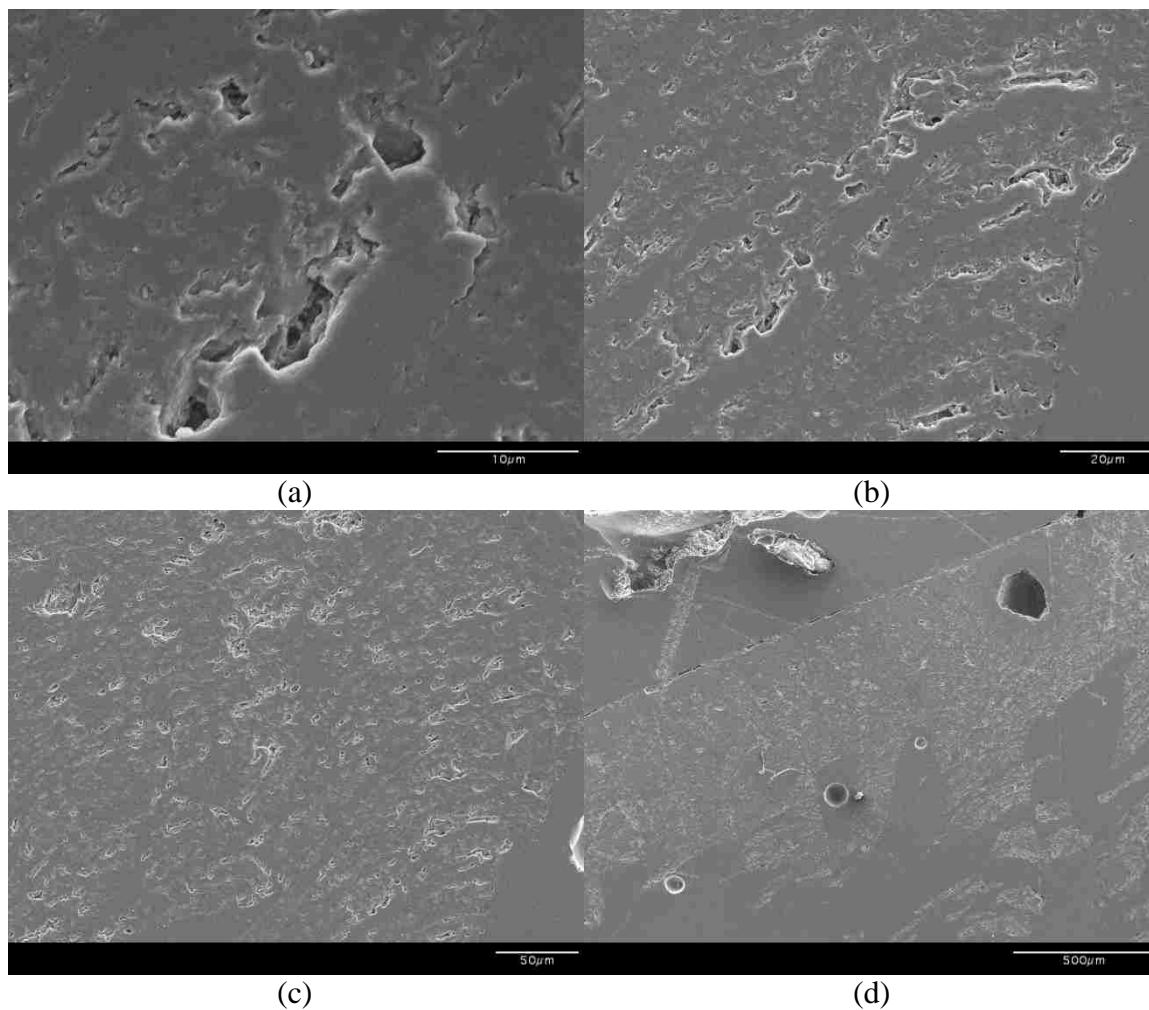
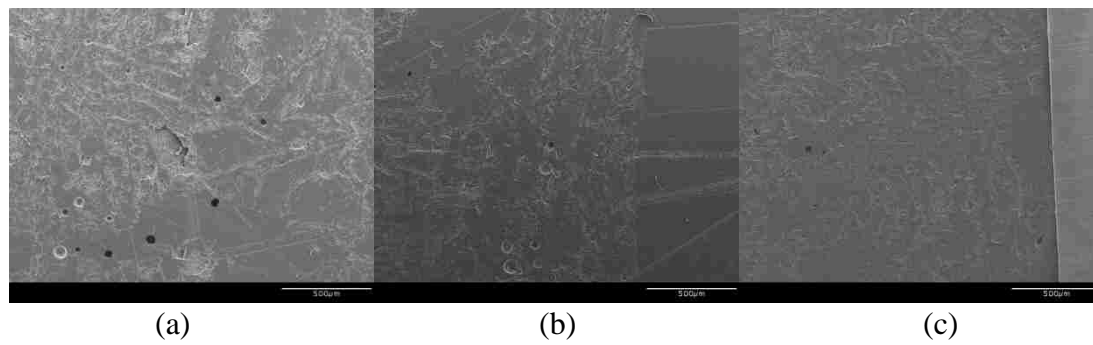
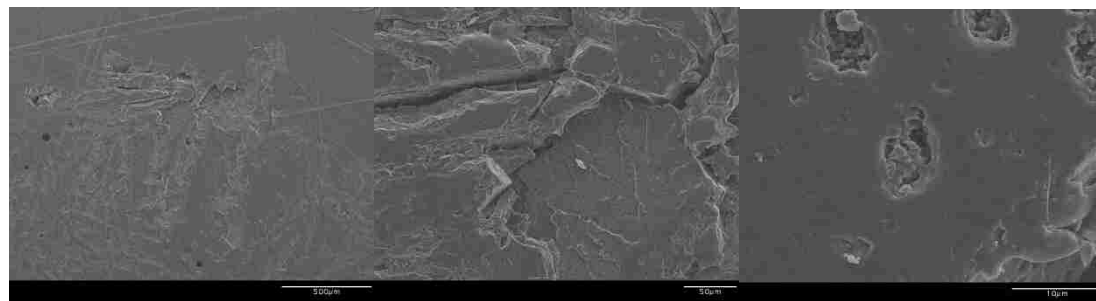


Figure B.7: SEM Images of Freeze-Cast Bar #2 of the Aquazol Additive Group: (a) 3000X Zoom; (b) 1000X Zoom; (c) 350X Zoom; (d) 60X Zoom;





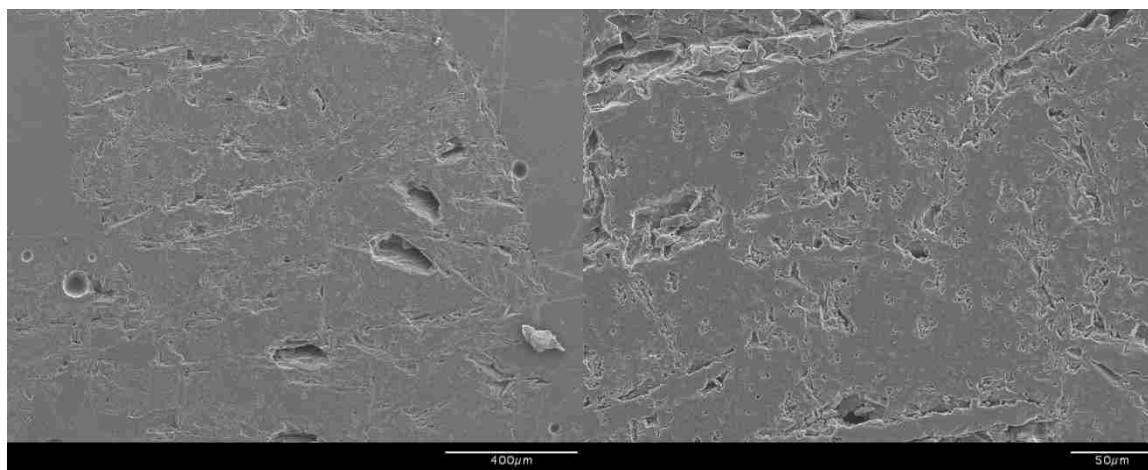


(d)

(e)

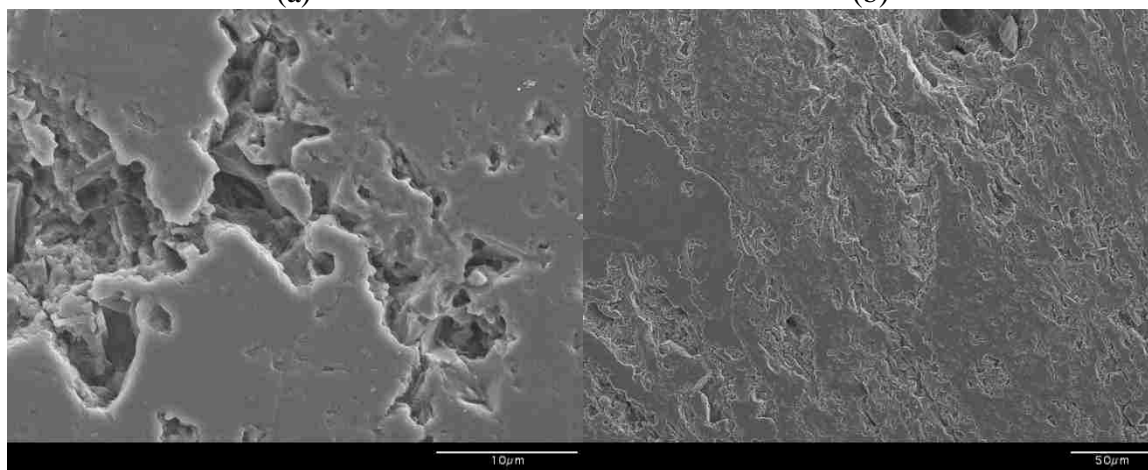
(f)

Figure B.8: SEM Images of Freeze-Cast Bar #2 of the Control Old Additive Group: (a) 60X Zoom; (b) 60X Zoom; (c) 60X Zoom; (d) 60X Zoom; (e) 350X Zoom; (f) 3000X Zoom



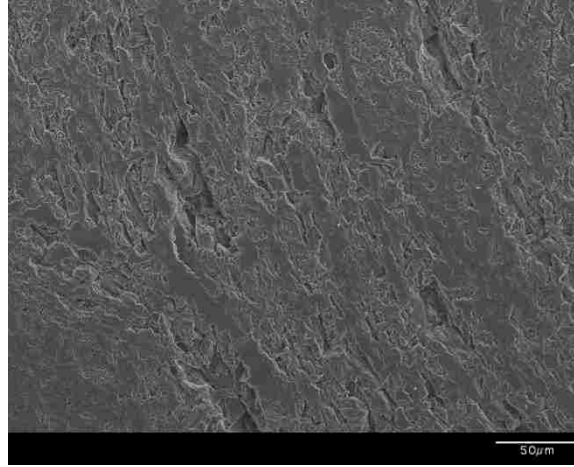
(a)

(b)



(c)

(d)



(e)

Figure B.9: SEM Images of Freeze-Cast Bar #1 of the Control New Additive Group: (a) 70X Zoom; (b) 350X Zoom; (c) 3000X Zoom; (d) 350X Zoom; (e) 350X Zoom;

APPENDIX C.

OTHER ADDITIVES CONSIDERED DURING THE STUDY

A bacteria named *Pseudomonas Syringae* was considered as a possible additive to the test slurry. This bacteria contains a protein coating which promotes ice nucleation at temperatures normally considered warm for efficient ice nucleation. It was found that concentrations of  $10^6$  was most suitable for nucleating ice at temperatures between  $-1.8^\circ$  and  $-3.8^\circ$  C [22]. This bacteria may be a good additive to solve the ice-crystal void problem occurring in the B<sub>4</sub>C parts fabricated by the FEF process. Due to accessibility and time constraints this bacteria was not included as an additive in this study.

Montmorillonite and Kaolinite were also considered as possible additives to the test slurry. These substances in mineral dust form have been used in an aerosol for cloud seeding. In the aerosol form they have been shown to efficiently nucleate ice [23]. These mineral dusts could be good additives to solve the ice-crystal void problem occurring in the B<sub>4</sub>C parts fabricated by the FEF process. Due to accessibility and time constraints they were not included as an additive in this study.

Silver iodide was also considered as a possible additive to the test slurry. Silver iodide may serve as a very effective nucleus because it very closely resembles ice in crystal structure. Both dimensions of the unit cell of ice and silver iodide are the same to within approximately one percent. It was shown that silver iodide could act as an efficient ice nucleation point up to  $-4^\circ$  C for particles one micron in diameter [24]. Silver iodide could be a good additive to solve the ice-crystal void problem occurring in the B<sub>4</sub>C parts fabricated by the FEF process. Due to accessibility and time constraints it was not included as an additive in this study.

APPENDIX D.

RECIPE FOR TEST SLURRY

The test slurry follows the recipe for B<sub>4</sub>C paste except that for the purposes of reducing processing time the ball-milling step was removed and no methocell was added. The following recipe would be for a full batch of paste. In order to save powder and other materials the test slurry could be made in one-half batches or 3/8 batches by proportioning all of the ingredients accordingly.

The required materials and amounts are:

- 300 grams of grade HD 20 B<sub>4</sub>C powder (washed with methanol to remove any borate).
- 2.4 grams of TMAH
- 120 milliliters of de-ionized water
- Appropriate amount of the desired additive:
  - Alumina was added in 1 wt% of the B<sub>4</sub>C powder (3 grams for a full batch, 1.5 grams for a half batch)
  - Aquazol 5: added 4 grams
  - BYK 348: added 3.6 grams (1mg of BYK per 1 m<sup>2</sup> surface area of powder)
  - BYK 349: added 3.6 grams
  - Glycerol: example of 25 wt% by water:  $\frac{x}{x+y} = 0.25$  and  $\frac{x}{D_G} + y = 120 \text{ ml}$

The above calculation is a two-equation system with two-unknowns which must be solved simultaneously. X is the weight of glycerol to be added, y is the weight or volume of water to be added (since pure water has a density of 1), D<sub>G</sub> is the accepted value of the density of glycerol which is 1.261 g/cm<sup>3</sup>, 120 is the total amount of fluid volume, and 0.25 is the desired % concentration.

Pour the de-ionized water into a jacketed beaker with the mixer running inside. Initially the mixer should be running at a slow speed. Slowly add the TMAH to the mixing water and allow it to dissolve completely (approximately 20-30 seconds). Next the additive should be added: glycerol in its appropriate amount, or alumina, etc. If the additive is aquazol, it is added last when the jacketed beaker is heated to at least 70<sup>0</sup>C. After the additive has been added slowly add the B<sub>4</sub>C powder. This process typically takes 5-10 minutes. By this point the B<sub>4</sub>C powder had been washed with methanol in order to remove any borate that may have formed on the surface of the powder particles. A little bit of powder should be added and then the setup should be allowed to mix until the recently added powder is visibly mixed into the slurry. As more and more powder is added it will take longer and longer for the recent addition of powder to mix into the

slurry. As more powder is added the speed of the mixer can be increased. Once all of the powder has been mixed into the slurry allow it to mix for 10-15 minutes to ensure that the slurry mixes homogenously.


Next, pour or spoon the slurry into a whip-mix container. The slurry should be whip-mixed for 5 minutes, then 3 minutes, then two minutes, taking at least a two minute break in between cycles. The whip-mixing helps remove any dissolved gas from the slurry preventing bubbles in finished parts.

Typically the jacketed beaker is not heated. At high concentrations of glycerol the slurry gets really thick and viscous at room temperature. For the glycerol concentrations of 20% and 25% the beaker should be heated to 40<sup>0</sup>C to help decrease the viscosity of the slurry. The aquazol requires heat in order to dissolve into water. Thus, the jacketed beaker should be heated to 70<sup>0</sup>C before the aquazol is added.

## 6. BIBLIOGRAPHY

- [1] Thévenot, F., 1990, "Boron carbide—A Comprehensive Review," *Journal of the European Ceramic Society*, 6 (4), pp. 205-225.
- [2] AZO Materials Website, May 2014. "Beryllium – Mechanical Properties and Material Applications," <http://www.azom.com/article.aspx?ArticleID=7646>.
- [3] Center for Disease Control Website, May 2014. "Beryllium Compounds (as Be) ," <http://www.cdc.gov/niosh/idlh/7440417.html>.
- [4] Cesarano, J., 1998, "A Review of Robocasting Technology," *MRS Proceedings*, 542, pp. 133.
- [5] Cai, K., Roman-Manso, B., Smay, J., Zhou, J., Osendi, M., Belmonte, M., Miranzo, P., 2102, "Geometrically Complex Silicon Carbide Structures Fabricated by Robocasting," *J. Am. Ceram. Soc.*, 95 (8), pp. 2660–2666.
- [6] Yoo, J., Cima, M.J., Khanuja, S., Sachs, E. M., 1993, "Structural Ceramic Components by 3D Printing," *Proceedings of the Solid Freeform Fabrication Symposium*, Austin, TX, pp. 40-51.
- [7] Melcher, R., Martins, S., Travitzky, N., Greil, P., 2006, "Fabrication of Al<sub>2</sub>O<sub>3</sub>-based Composites by Indirect 3D-printing," *Materials Letters*, 60 (4), pp. 572-575.
- [8] Liu, Z., Nolte, J., Packard, J., Hilmas, G., Dogan, F., Leu, M. C., 2007, "Selective Laser Sintering of High-density Alumina Ceramic Parts," *Proceedings of the MATADOR Conference*, Taipei, Taiwan, pp. 351-354.
- [9] He, G., Hirschfeld, D., Cesarano III, J., Stuecker, J., 2000, "Processing of Silicon Nitride-Tungsten Prototypes," *Ceramic Transactions*, 114, pp. 325-332.
- [10] Huang, T., Mason, M.S., Hilmas, G., Leu, M.C., 2006, "Freeze-form Extrusion Fabrication of Ceramic Parts," *International Journal of Virtual and Physical Prototyping*, 1 (2), pp. 93-100.
- [11] Mason, M.S., Huang, T., Landers, R., Leu, M.C., Hilmas, G., 2009, "Aqueous-Based Extrusion of High Solids Loading Ceramic Pastes: Process Modeling and Control," *Journal of Materials Processing Technology*, 209 (6), pp. 2946-2957.



- [12] Huang, T., Mason, M.S., Hilmas, G., Leu, M.C., 2009, "Aqueous Based Freeze-form Extrusion Fabrication of Alumina Components," *Rapid Prototyping Journal*, 15 (2), pp. 88-95.
- [13] Zhao, X., Landers, R., Leu, M.C., 2010, "Adaptive Extrusion Force Control of Freeze-Form Extrusion Fabrication Processes," *ASME Journal of Manufacturing Science and Engineering*, 132 (6), pp. 064504.
- [14] Li, X., Jiang, D., Zhang, J., Lin, Q., Chen, Z., Huang, Z., 2013, "The Dispersion of Boron Carbide Powder in Aqueous Media," *Journal of the European Ceramic Society*, 33 (10), pp. 1655-1663.
- [15] Sofie, S., Dogan, F., 2001, "Freeze Casting of Aqueous Alumina Slurries with Glycerol," *Journal of the American Ceramic Society*, 84 (7), pp. 1459–1464.
- [16] Huang, T., 2007, "Fabrication of Ceramic Components Using Freeze-form Extrusion Fabrication," *Dissertation*, Rolla, Missouri.
- [17] Li, A., 2012, "Research Report on Boron Carbide," *Research report submitted to Lockheed Martin*, Rolla, Missouri. 
- [18] Fletcher, N., 1958, "Size Effect in Heterogeneous Nucleation," *Journal of Chemical Physics*, 29, pp. 572.
- [19] Wachtman, J., 1996, "Mechanical Properties of Ceramic Materials," *John Wiley & Sons, Inc.*, pp. 56.
- [20] Green, D., 1998, "An Introduction to the Mechanical Properties of Ceramics," *Cambridge University Press*, pp. 225-226.
- [21] Lane, L., 1925, "Freezing Points of Glycerol and its Aqueous Solutions," *Industrial & Engineering Chemistry*, 17 (9), pp. 924-924.
- [22] Maki, L., Galyan, E., Chang-Chen, M., Caldwell, D., 1974, "Ice nucleation induced by *Pseudomonas Syringae*," *Applied Microbiology*, 28 (3), pp.456-459.
- [23] Zuberi, B., Bertram, A., Cassa, C., Molina, L., Molina, M., 2002, "Heterogeneous Nucleation of Ice in  $(\text{NH}_4)_2\text{SO}_4\text{-H}_2\text{O}$  Particles with Mineral Dust Immersions," *Geophysical Research Letters*, 29 (10), pp.142-1 – 142-4.

[24] Vonnegut, B., 1947, "The Nucleation of Ice Formation by Silver Iodide," *Journal of Applied Physics*, 18, pp. 593-595.

## VITA

Aaron Scott Thornton was born on August 31, 1985. He earned his Bachelors of Science in Mechanical Engineering from the Missouri University of Science and Technology in May 2011. He earned his Masters of Science in Mechanical Engineering from the Missouri University of Science and Technology in August 2015.